Calcium and Elongated Grains in Alumina

Iman Naamne

Calcium and Elongated Grains in Alumina

Research Thesis

In Partial Fulfillment of The

Requirements for the Degree of

Master of Science in Materials Engineering

Iman Naamne

Submitted to the Senate of the Technion-Israel Institute of Technology

Tishri 5785 Haifa October 2024

The research thesis was done under the supervision of Prof. Wayne D. Kaplan in the Department of Materials Science & Engineering**.**
This research was partially supported by the Israel Science Foundation (Grant No. 2070586)

The author of this thesis states that the research, including the collection, processing and presentation of data, addressing and comparing to previous research, etc., was done entirely in an honest way, as expected from scientific research that is conducted according to the ethical standards of the academic world. Also, reporting the research and its results in this thesis was done in an honest and complete manner, according to the same standards.

Table of Contents

List of Figures ..... **V**

List of Tables ..... **VII**

Abstract **1**

List of Symbols and Abbreviations **2**

1. Literature Survey **4**

1.1 Ceramics Processing **4**

1.1.1 Solid State Sintering 4

1.2 Grain Growth (Grain Boundary Mobility) **6**

1.2.1 Driving Force for Grain Growth 6

1.2.2 Mechanisms of Grain Growth 7

1.2.3 The Influence of Dopants on Grain Boundary Mobility 9

1.2.4 Abnormal Grain Growth 12

1.2.5 Measuring the Grain Boundary Mobility 13

1.3 Alumina **13**

1.3.1 α-Alumina Structure 13

1.4 Grain Boundary Mobility in Alumina **15**

1.4.1 Grain Boundary Mobility in MgO-Doped Alumina 15

1.4.2 Grain Boundary Mobility in Ca-Doped Alumina 16

1.4.1 Complexions in Alumina 17

1.4.2 Single Crystal Growth into Ca-doped Alumina 18

1.5 Equilibrium Crystal Shape **19**

1.5.1 Surface Energy and Wulff Construction 19

1.5.2 The Equilibrium Crystal Shape of Undoped Alumina 22

1.5.3 Ca Segregation to Grain Boundaries 24

2. Research Goals **25**

3. Experimental Methods **26**

3.1 Sample Preparation **26**

3.1.1 Undoped and Ca-Doped Polycrystalline Alumina 26

3.1.2 Diffusion Bonding 27

3.1.3 Focused Ion Beam – Fabrication of Holes and Needles 27

3.2 Characterization Methods **28**

3.2.1 Density 28

3.2.2 Wavelength Dispersive Spectroscopy 28

3.2.3 Scanning Electron Microscopy 30

3.2.4 Grain Size Analysis 30

3.2.5 Measuring the Effective Mobility of Single Crystal Sapphire 31

3.2.6 Time to Reach Equilibrium 32

3.2.7 Electron Back-Scattered Diffraction 32

3.2.8 Focused Ion Beam Cross-Sectioning 32

4. Results **34**

4.1 Dopant and Impurities Content **34**

4.2 Density and Microstructure 35
4.2.1 Undoped Alumina 35
4.2.2 Ca-Doped Alumina 35

4.3 Effective Grain Boundary Mobility of Alumina at 1600ºC 36
4.3.1 Morphology and Effective Grain Boundary Mobility Measured from the Bulk vs. from the Surface 38

4.4 Anisotropic Grain Boundary Mobility of Alumina at 1600ºC 40

4.5 The Equilibrium Crystal Shape of Alumina 43
4.5.1 Time Required to Reach Equilibrium 43
4.5.2 Relative Surface Energy Estimated from Internal Cavities in Ca-Doped Alumina 45
4.5.3 Relative Surface Energy Estimated from Internal Cavities in Undoped Alumina 50

5. Discussion 53

5.1 Grain Boundary Motion 53
5.1.1 Effective Grain Boundary Mobility of Undoped and Ca-Doped Alumina 53
5.1.2 The Effect of Surface on Grain Size Measurements and Grains Morphology 58
5.1.3 Anisotropic Grain Boundary Mobility of Ca-Doped Alumina 59
5.1.4 The Mobility of the Basal Plane (0001) 60
5.1.5 The Mobility of Non-Basal Planes 60
5.1.6 Sapphire Single Crystal Morphology at the Interface of Diffusion Bonded Samples 61

5.2 The Equilibrium Crystal Shape of Ca-Doped Alumina. 62

6. Summary and Conclusions 64

7. Recommendations for Future Work 65

8. References 66

List of Figures

Figure 1: Schematic illustration of densification and grain growth during sintering, reproduced after [1]. 4

Figure 2: Schematic illustration of transport mechanisms during sintering; reproduced after [2]. 6

Figure 3: Schematic drawing of atom motion (or reorientation) from one grain to the other and the movment of (a) a curved grain boundary and (b) a faceted grain boundary. 7

Figure 4: Schematic illustration showing the TLK model for crystal growth; terraces, ledges (steps), kinks (reproduced after [10]). 8

Figure 5: Schematic drawing of solute profile around the grain boundary, (reproduced after [2]) 9

Figure 6: Driving force and velocity behavior for (a) intrinsic mobility (b) solute drag only and (c) total force velocity, (redrawn after [11]). 10

Figure 7: Schematic description of Zener effect, where a spherical second phase particle, or a pore, induces a drag force on the grain boundary, reproduced from [2]. 11

Figure 8: Pore boundary interaction as a function of grain and pore size, assuming pores migrate by surface diffusion [17]. 12

Figure 9: Schematic drawing of the hexagonal (a) and rhombohedral (b) unit cells of α-alumina. The blue spheres represent aluminum cations, and the red spheres represent oxygen anions [20]. 14

Figure 10: Schematic illustration of the crystallographic planes of alumina. 15

Figure 11: SEM micrograph showing abnormal and elongated growth in alumina doped with ~ 350 ppm Ca [16]. 17

Figure 12: Grain boundary mobilities for different complexions in normal and abnormal grains in Ca-doped alumina [12]. 18

Figure 13: Typical polar plot of a crystal surface, (reproduced from []). 20

Figure 14: Wulff shape constructed using γ-plot, (reproduced from [35]). 21

Figure 15: TEM micrographs of two different cavities in an *A*- oriented specimen annealed at 1600C for 50 h in air. The zone axes are (a) [**2110**], (b) [**1010**] [22]. 22

Figure 16: Simulated cavity shape using anisotropic surface energy [22]. 23

Figure 17: SEM micrograph of a pore exposed parallel to the *A*-plane after 480 h at 1600°C [25]. 23

Figure 18: Schematic illustration of the diffusion bonding experimental configuration. 27

Figure 19: Secondary electron (SE) SEM micrographs (polished and thermally etched cross-sections) of undoped alumina microstructure annealed in air at 1600°C for (a) 0 h, and (b) 8 h. 35

Figure 20: SE SEM micrographs (polished cross-sections) of Ca-doped alumina microstructure, annealed in air at 1600°C for (a) 0 h, and (b) 4 h. In (b) the small (alumina) particles at the grain boundaries are from the thermal annealing process. 36

Figure 21: SE SEM micrographs (polished cross-sections) of Ca-doped alumina microstructure, annealed in air at 1600°C for (a) 8 h, and (b) 10 h. 36

Figure 22: Grain growth kinetics of *undoped* alumina and, 15 ppm *Ca-doped* alumina samples annealed at 1600°C in air. The slopes represent the values of the effective mobility of the different samples, and the error bars represent the standard error. 37

Figure 23: SE SEM micrographs (polished cross-sections) of Ca-doped alumina, annealed in air at 1600°C. (a)-(c) present the microstructure of the surface, after 2, 4 and 10 hr of annealing, respectively. (d)-(f) present the microstructure of the bulk after 2, 4 and 10 hr of annealing, respectively. . 38

Figure 24: Grain growth kinetics of Ca-doped alumina samples annealed at 1600°C in air, measured from the surface and from the bulk. The slopes represent the values of the effective mobility of the different area of measurement. 39

Figure 25: SE SEM micrographs of displacement of (a) *C* – oriented sapphire diffusion bonded to *Ca-doped* alumina at 1600°C for 50 h, and (b) *A* – oriented sapphire diffusion bonded to *undoped* alumina at 1600°C for 20 h. The interface between the single crystal and polycrystalline material is indicated by a white line, where the original interface (before crystal growth) is delimited by residual pores. 41

Figure 26: Grain growth kinetics of the *C*, *A*, and *R* – oriented single crystals sapphire diffusion bonded to *undoped* alumina at 1600°C. 42

Figure 27: Grain growth kinetics of the *C*, *A*, and *R* – oriented single crystals sapphire diffusion bonded to *Ca-doped* alumina at 1600°C. 42

Figure 28: SE SEM micrographs of a hole fabricated in polycrystalline Ca-doped alumina annealed in air at 1600°C for (a) 3 h, (b) 11 and (c) 23 h. 44

Figure 29: Ratio ***LALB*** as a function of time, for a hole annealed at 1600°C. The dashed line is only a guide to the eye. 44

Figure 30: EBSD map in polycrystalline Ca-doped alumina sample. An A-oriented grain, in which a hole was fabricated, is indicated with a white rectangle. . 45

Figure 31: SE SEM micrographs of a hole in an A-oriented polycrystalline Ca-doped alumina grain, annealed at 1600°C for 20 h. 46

Figure 32: SE SEM micrographs of a cross-section of the annealed hole. The observed facets and their perpendiculars are marked. 46

Figure 33: A simulation of the ECS of undoped alumina, produced using Krystal Shaper software, using relative surface energies reported from the literature [22]. 47

Figure 34: SE SEM micrographs of a hole in a grain in polycrystalline Ca-doped alumina, annealed at 1600°C for 20 h. 48

Figure 35: SE SEM micrographs of the cross-section of the annealed hole in Figure 34. The observed facets and their normal are marked. 49

Figure 36: SE SEM micrographs of a cross-section of an annealed hole in undoped alumina. The observed facets and their normal are marked. 51

Figure 37: Schematic showing the effect of different amounts of disorder within the core of a grain boundary on the grain-boundary mobility, reproduced after [12]. 54

Figure 38: (a) Schematic drawing of a general grain boundary in a polycrystalline matrix presenting (a) ideal system with no segregation, with one type of disconnection, and (b) adsorption to the grain boundary resulting in additional type of disconnection (D_2) 55

Figure 39: Schematic drawing of effective grain boundary mobility as a function of dopant concentration for a single grain boundary in a polycrystalline matrix. 56

Figure 40: Averaged effective grain boundary mobility as a function of adsorbing dopant concentration in a polycrystalline system. 57

List of Tables

Table 1: Summary of the dopant/impurity concentrations in the samples produced for this study. 34

Table 2: Summary of the effective single crystal mobility measured for undoped, and Ca-doped alumina at 1600°C. 43

Table 3: Summary of the identified facets and their estimated relative surface energies. 47

Table 4: Summary of the identified facets and their estimated relative surface energies for the hole presented in Figure 35. 49

Table 5: Summary of the identified facets and their estimated relative surface energies for the hole presented in Figure 36, calculated from intersection point O_1. 51

Table 6: Summary of the identified facets and their estimated relative surface energies for the hole presented in Figure 36, determined from intersection point O_2. 51

Abstract

Grain growth is a critical process accompanying densification during the sintering of polycrystalline ceramics, where the resulting grain morphology can significantly influence material properties.

One of the most studied ceramic materials is α-alumina (α-Al_2O_3), commonly used as a model system due to its optical and mechanical properties. Many studies in alumina have showed that dopants and/or impurities can cause significant changes to the grain boundary mobility of materials, affecting grain growth kinetics and morphology, this can occur by equilibrium (Gibbsian) segregation of solutes to grain boundaries, which is driven by a reduction in grain boundary energy.

It has been shown that calcium (Ca) in alumina, at a concentration below solubility limit, leads to anisotropic and accelerated grain boundary mobility, forming elongated, plate-like grains. It is not clear if the elongated shape is due to the system approaching equilibrium, i.e. the equilibrium crystal shape (ECS) due to adsorbed Ca to some crystallographic surfaces, or if this is a kinetic shape where Ca causes anisotropic grain boundary mobility.

In this work, the ECS of Ca-doped alumina was studied using internal cavities. Combined ion and electron microscopy techniques were used to introduce initial cavities, to determine that equilibrium had been reached, and to analyze the equilibrated cavities to determine the ECS of Ca-doped alumina. The rate of motion of the interface of oriented single crystals of sapphire into Ca-doped polycrystalline alumina was used to derive the anisotropic grain boundary mobility, demonstrating that Ca influences the kinetics of grain boundary mobility and not only the grain boundary energy.

List of Symbols and Abbreviations

A	Area of the interface inside the interaction volume
AFM	Atomic force microscopy
Ca	Calcium
$C_{lim,0.975}$	Limit of detection at confidence probability of 97.5%
C_{std}	Concentration within the standard
C_∞	Bulk solute concentration
D	Dry weight
EBSD	Electron backscatter diffraction
ECS	Equilibrium crystal shape
EDS	Energy dispersive spectroscopy
FIB	Focused ion beam
F_{GB}	Driving force for grain boundary movment
F_z	Zener drag force
F_p	Pore Zener drag force
G	Grain size
GB	Grain boundary
HRTEM	High resolution transmission electron microscopy
I_{sample}, I_{std}, I_{bgd}	Measured X-ray intensity from the unknown sample, the standard and the background, respectively.
IGF	Intergranular films
$\bar{L}$	Average intercept length
$\overline{\Delta L}$	Average displacement
l_1, l_2	Distance between the Wulff point and the surface of the substrate and between the Wulff point and one of the facets of the particle, respectively
M_{GB}	Grain boundary mobility
M_p	Pore mobility
M_s	Single crystal mobility
N_z	Number of particles/ pores
Mg	Magnesium

P	Confidence of probability
ppm	Parts per million
ΔP	Pressure difference
S	Surface entropy
S	Suspended weight
SE	Secondary electrons
SEM	Scanning electron microscopy
Si	Silicon
STEM	Scanning transmission electron microscopy
T	Temperature
T_m	Melting temperature
TEM	Transmission electron microscopy
V	Interaction volume
V_{GB}	Grain boundary velocity
V_p	Pore velocity
W	Saturated weight
WDS	Wavelength dispersive spectroscopy
WMC	Weighed mean curvature
XRD	X-ray diffraction
α_s	Solute drag force per unit velocity per unit solute concentration
Γ	Surface excess of solute
γ	Surface or interface energy
ρ	Matrix density in atoms/nm^3
τ	Single measurement time
τ_{eq}	Equilibration time
k_1	Rate constant
$\bar{G}$	Average grain size
n	Geometrical factor for grains geometry
θ	Dihedral angle
μ	Chemical potential
f	Degree of freedom
σ_{bgd}	Standard deviation of the background

1. Literature Survey

1.1 Ceramics Processing

1.1.1 Solid State Sintering

Ceramics are known for their high melting points, which makes them challenging to melt and cast using conventional methods. To process a ceramic material, a green body, made by compacting ceramic powder, is subjected to thermal energy that is typically between 50% and 80% of the material's melting temperature (T_m). This heat treatment provides sufficient atomic mobility for the material to undergo densification. The driving force behind the sintering process is the reduction of surface excess energy, as described by Equation (1):

$$\Delta(\gamma A) = \Delta\gamma A + \gamma\Delta A \quad (1)$$

where γ represents the surface/interface energy, A is the total surface/interface area, and γA is the total surface/interface energy.

During the sintering process, two competing phenomena occur simultaneously, densification and grain growth, as illustrated in Figure 1.

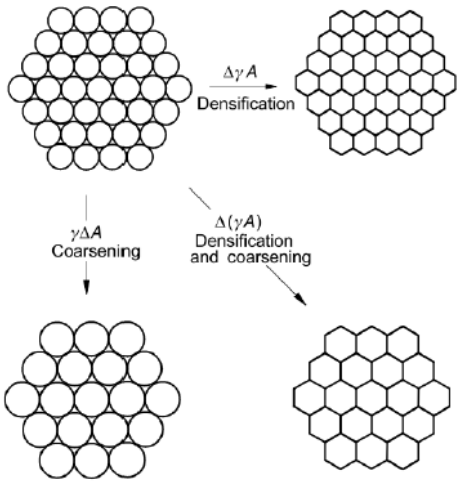

Figure 1: Schematic illustration of densification and grain growth during sintering, reproduced after [1].

The first phenomenon is densification, where the free surface of the particles is replaced by grain boundaries. Since grain boundaries usually have a lower excess energy

compared to free surfaces, this replacement leads to a reduction in $\Delta\gamma$, effectively lowering the overall energy of the system.

Grain growth, also known as coarsening, is the second phenomenon that takes place during sintering. In this process, the specific excess surface energy remains unchanged (ignoring changes in facets), but the total grain boundary area ΔA decreases. As a result, the total energy in the system, represented by γA, is reduced.

When densification is dominate, the density of the compact powder increases via the elimination of pores. This occurs as the particles join and the free space between them is reduced, resulting in a denser and more cohesive material. On the other hand, when grain growth dominates the sintering process, both the particles and pores within the ceramic will increase in size over time, leading to larger grains and pores, which can negatively impact the mechanical properties and performance of the sintered ceramic. In this case, the ceramic may exhibit lower density and reduced strength compared to a material where densification is the primary process.

1.1.1.1 Mass Transfer Mechanism

During sintering, mass transfer occurs from regions of high chemical potential (sources) to regions of lower chemical potential (sinks or necks) through diffusion. This transfer can occur via several mechanisms: (1) surface diffusion, (2) lattice/volume diffusion, or (3) evaporation-condensation through a gas phase to the neck. Mass can also transfer along the grain boundaries via (4) grain boundary diffusion, or (5) viscous flow. These different mechanisms are presented in Figure 2, for a simple model of three spherical particles.

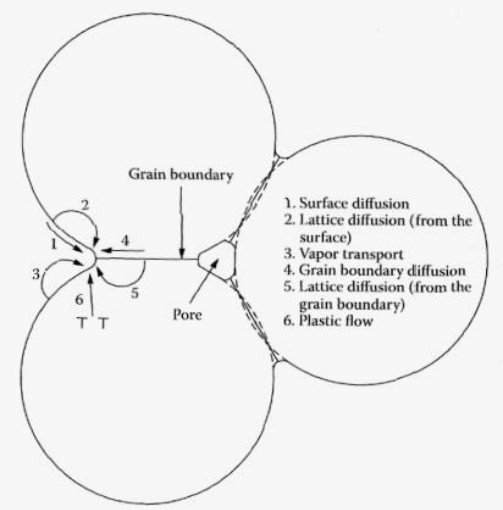

Figure 2: Schematic illustration of transport mechanisms during sintering; reproduced after [2].

1.2 Grain Growth (Grain Boundary Mobility)

1.2.1 Driving Force for Grain Growth

During sintering, most grain growth takes place during the final stages of densification. To reduce the grain boundary area and thereby lower the system's excess energy, grain boundaries (GB) migrate. This process involves short-range motion of atoms, where atoms reorient from that of the shrinking crystal to that of the expanding grain. As a result, the atomic flux is in the opposite direction of the grain boundary movement (as shown in Figure 3). The driving force behind this migration is typically described by the curvature of the grain boundary, which induces a chemical potential difference due to the pressure variation between the two grains, causing convex grains to have a higher chemical potential than concave grains:

$$\Delta P = \gamma_{GB}\left(\frac{1}{r_1}+\frac{1}{r_2}\right) = \frac{n\gamma_{GB}}{\bar{G}} \qquad (2)$$

where ΔP is the pressure difference between adjacent grains, γ_{GB} is the grain boundary energy, n is a geometrical factor, $\bar{G}$ is the grain size, and r_1 and r_2 are the principal radii of curvature at a given point on the interface between two grains.

Grain boundaries are not completely curved, but usually faceted, meaning their surfaces consist of flat planes parallel to crystallographic planes. As a result, it is common to use the concept of weighted mean curvature (WMC), which also shows that elimination of

grain boundary area (and thus excess energy) results from the motion of grain boundaries in the direction of the weighted mean curvature [3].

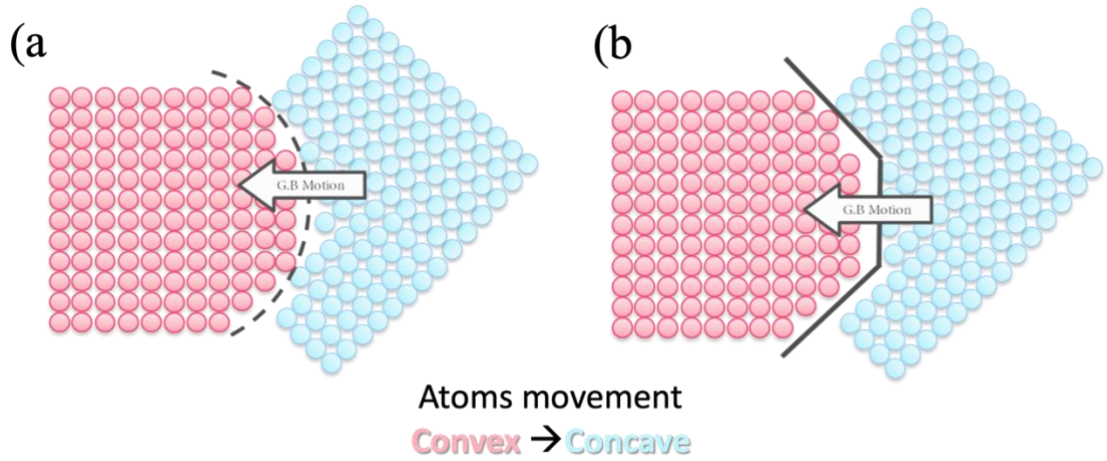

Figure 3: Schematic drawing of atom motion (or reorientation) from one grain to the other and the movment of (a) a curved grain boundary and (b) a faceted grain boundary.

Recent work by Battacharya et al. demonstrated by very careful X-ray microscopy experiments on nickel, that there is no correlation between curvature and the direction of crystal growth, or even as a driving force [4]. Their experimental study found that the velocity of the grain boundaries was strongly correlated with crystallographic properties of the grains and may be influenced by defect-mediated migration or anisotropy of grain boundary energy.

In another work by Muralikrishnan et al. on strontium titanate, flat boundaries were found to move faster than curved boundaries, and 37% of all measured boundaries moved in the direction opposite to their curvature [5].

These unexpected observations suggest that in materials with anisotropic grain boundary properties, mechanisms other than curvature-driven boundary migration play a role in the minimization of interfacial energy, which is the only driving force for grain growth.

1.2.2 Mechanisms of Grain Growth

The atomistic mechanism by which atoms migrate a length which is less than an interatomic distance was first suggested by Gleiter using the terrace-ledge-kink (TLK) model for surfaces (Figure 4) [6]. The TLK model was originally developed for crystal

surfaces and cannot be directly applied to interfaces in crystalline materials. This is because interfacial line defects are not pure steps/ledges; they are, in general, characterized by both a step height and a Burgers vector. These line defects are in fact disconnections and their movement along the GB is the main mechanism by which a GB moves and results in grain growth [7]. This was experimentally demonstrated by Sternlicht et al. for strontium titanate, and Han et al. have recently extensively modeled the role of disconnections in grain growth [8,9].

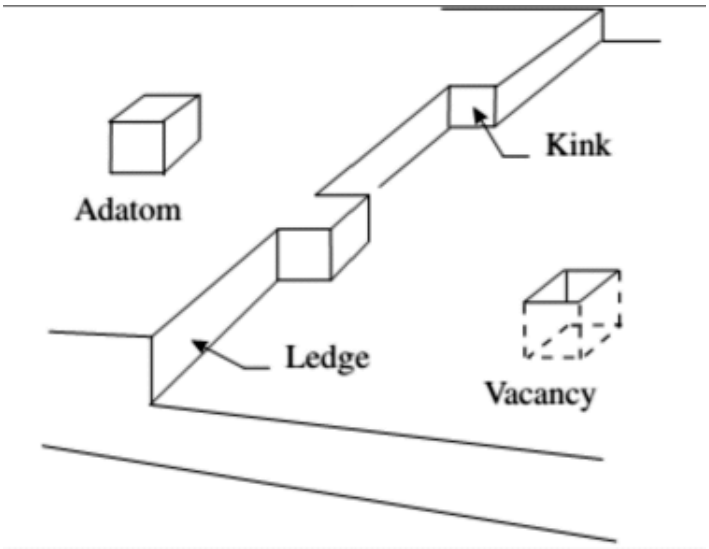

Figure 4: Schematic illustration showing the TLK model for crystal growth; terraces, ledges (steps), kinks (reproduced after [10]).

In a single-phase system, grain boundaries migrate with a velocity V_{GB}, due to a driving force F_{GB} (which was until recently assumed to be curvature). Ignoring curvature and assuming grain size defines the driving force, this will vary with annealing time and for different systems. Therefore, in order to be able to compare between systems, the normalized velocity called grain boundary mobility, M_{GB} is used to describe the grain boundary relative velocity [10]:

$$\boldsymbol{M_{GB} = \frac{V_{GB}}{F_{GB}}} \qquad (3)$$

1.2.3 The Influence of Dopants on Grain Boundary Mobility

1.2.3.1 Solute Drag / Acceleration

Dopants or impurities in a polycrystalline material, at a concentration below their solubility limit, can undergo equilibrium (Gibbsian) segregation to the grain boundaries (or any surface in the system), which is driven by the reduction of the grain boundary energy. This segregation results in a solute concentration profile near the grain boundary which can interact with the atoms in and near the grain boundary core. When the grain boundary is stationary, the interaction will generate a symmetrical solute profile (ignoring deviation from symmetry due to the relative orientation of the two boundary delimiting crystals), resulting in a balanced interaction of forces on both sides of the boundary (Figure 5).

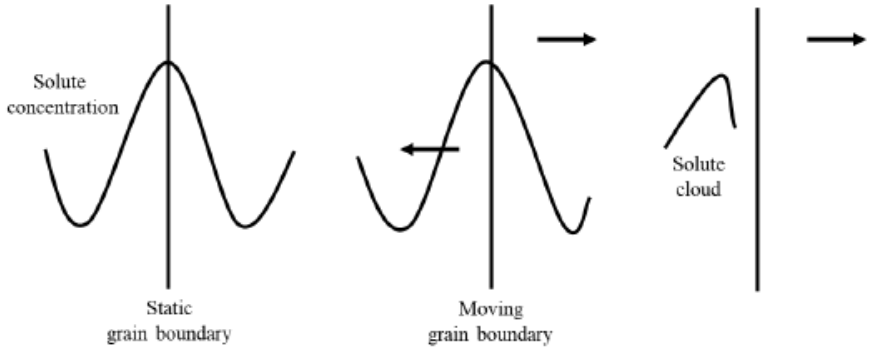

Figure 5: Schematic drawing of solute profile around the grain boundary, (reproduced after [2]) .

When the grain boundary starts moving (grain growth), the solute profile can become asymmetrical, due to the different diffusivity of the atoms across the grain boundary.

This asymmetry can result in a drag force F_s which can reduce the velocity of grain boundary migration. If the driving force for grain growth is high enough, the grain boundary can break away from the solute and return to its intrinsic mobility.

The magnitude of this drag force was calculated by Cahn as presented in Equation (4) [11] :

$$F_s = \frac{a_s C_\infty V_{GB}}{[1 + (\beta V_{GB})^2]} \tag{4}$$

where a_s is the solute drag force per unit velocity per unit solute concentration, C_∞ is the bulk solute concentration, and β is the drift velocity at which a solute diffuses across the grain boundary region. In steady state, the total drag force on a grain boundary is assumed to be the sum intrinsic drag force F_0 and the solute drag force F_s as described in Figure 6.

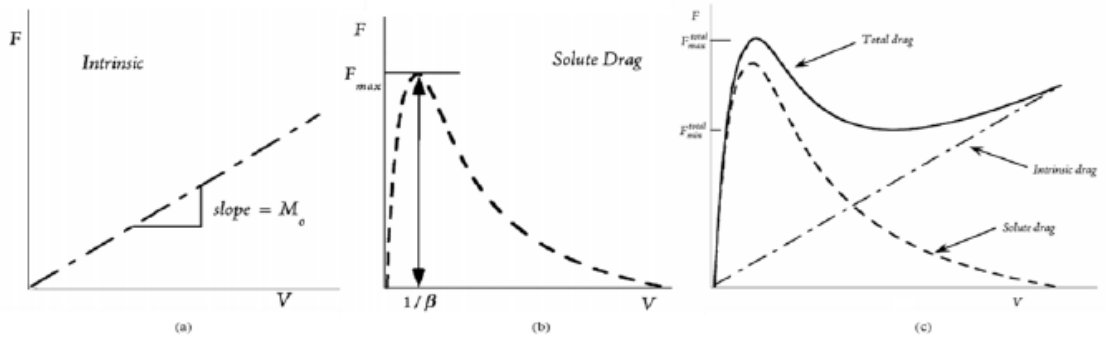

Figure 6: Driving force and velocity behavior for (a) intrinsic mobility (b) solute drag only and (c) total force velocity, (redrawn after [11]).

This theory shows that the solute presence near the grain boundary results in a drag effect, meaning a ***reduction*** in the grain boundary mobility. Recent experimental studies showed that the grain boundary mobility may also *increase* as a result of this solute profile [12-16].

1.2.3.2 Zener Drag

When dopants or impurities are present in a polycrystalline material at a concentration above their solubility limit, precipitation of a second phase occurs. The presence of the precipitates can pin the grain boundaries and hinder their motion by Zener drag [2]. This is also the case for the interaction of pores with grain boundaries. This effect was first considered by Zener, assuming that particles have a spherical shape and are insoluble, immobile and randomly distributed in the polycrystalline matrix, and induce a drag force on the grain boundary as a pinning force as shown in Figure 7.

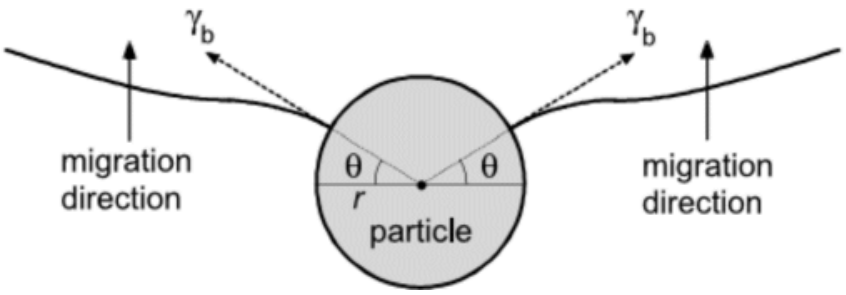

Figure 7: Schematic description of Zener effect, where a spherical second phase particle, or a pore, induces a drag force on the grain boundary, reproduced from [2].

The drag force of a single particle is expressed by:

$$F_z = \gamma_{GB} \sin(\theta) \cdot 2\pi r cos(\theta) = \pi r \gamma_{GB} \sin(2\theta) \quad (5)$$

where r is the spherical particle radius, and θ is the dihedral angle shown in Figure 7. When $\theta = 45°$, the drag force would be at maximum:

$$F_z^{max} = \pi r \gamma_{GB} \quad (6)$$

Having N_z particles or pores at the grain boundary, and combining with Equation (3), one can describe the grain boundary velocity under the Zener drag effect as:

$$V_{GB} = M_{GB}(F_{GB} - N_z \cdot F_z) \quad (7)$$

In a similar way, the velocity of a second phase particle or pore is:

$$V_p = M_p \cdot F_p \quad (8)$$

where M_p is the particle / pore mobility.

There are three cases of interaction between a particle / pore and a grain boundary (see Figure 8):

1. When $V_{GB} > V_p$, the particle / pore will be separated from the grain boundary.

2. When $V_{GB} = V_p$, the particle / pore will stay attached to the grain boundary, and the grain boundary velocity can be expressed as:

$$V_{GB} = F_{GB}\left(\frac{M_p M_{GB}}{N_z M_{GB} + M_p}\right) \quad (9)$$

In this case there are two possible conditions:

a. Pore control: when $N_z M_{GB} \gg M_p$, the grain boundary migration is limited by the particle / pore mobility.

b. Boundary control: when $N_z M_{GB} \ll M_p$, the grain boundary migration is not affected by the particle / pore mobility

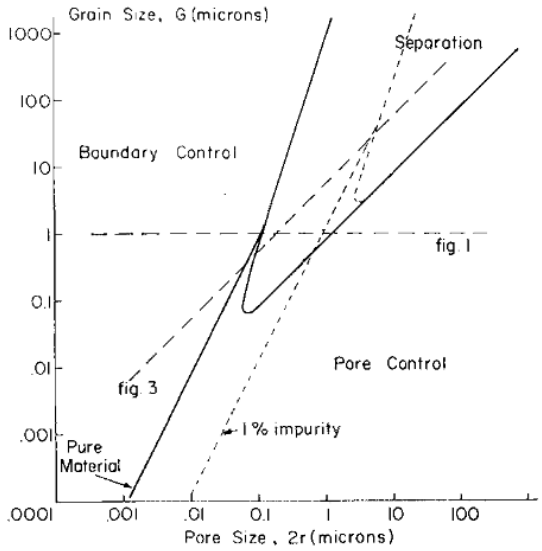

Figure 8: Pore boundary interaction as a function of grain and pore size, assuming pores migrate by surface diffusion [17].

1.2.4 Abnormal Grain Growth

Abnormal grain growth, or exaggerated grain growth, occurs when a few grains grow to a size significantly larger than the surrounding grains, often by an order of magnitude. This growth occurs at the expense of neighboring grains, driven by the higher grain boundary mobility of the abnormal grains. As these large grains expand, they are surrounded by more neighboring grains, typically more than six as noted by Hillert, leading to increased curvature at each boundary [18]. This increased curvature was believed to further accelerate the rapid growth of the abnormal grains at the expense of the surrounding ones.

In normal grain growth, the grain size distribution usually shows a single peak (unimodal distribution). In contrast, abnormal grain growth results in a bimodal distribution with two distinct peaks. While abnormal growth generally degrades the mechanical properties of a material and represents a significant microstructural change, the exact cause of this phenomenon remains unclear. It is often believed that second phases, such as particles or pores, and the presence of impurities locally suppress normal grain growth. As a result, only grains with grain boundaries exhibiting above-average curvature are able to migrate and grow, while the rest of the matrix maintains a uniform grain size. Recent studies have explored the relationship between intergranular films (IGFs) and the formation and growth of abnormal grains, documenting the presence of IGFs

experimentally. However, the influence of IGFs on grain boundary mobility is not fully understood and requires further investigation [1,19] .

1.2.5 Measuring the Grain Boundary Mobility

Measuring grain boundary mobility is a challenging task, particularly in ceramics, where it is impossible to completely eliminate impurities, since trace elements in the starting powder are unavoidable and achieving 100% pure ceramics is not possible. Despite these challenges, numerous studies have reported on grain boundary mobility in undoped samples, though they acknowledge the inherent limitations due to these impurities.

The velocity at which a grain boundary moves can be expressed as the change in the grain size with time:

$$V_{GB} = \frac{d\bar{G}}{dt} \tag{10}$$

Combining Equations (3) and (10), taking $\alpha = 2$ for equi-axed grains gives:

$$\frac{d\bar{G}}{dt} = \frac{2M_{GB}\gamma_{\mathrm{GB}}}{\bar{G}} \tag{11}$$

By integrating Equation (11) we obtain the following:

$$\bar{G_t}^{\,2} - \bar{G_0}^{\,2} = 4M_{GB}\gamma_{GB}t = k_1 t \tag{12}$$

where $\bar{G}_t$and $\bar{G}_0$ are the average grain size at t and 0, $M_{GB}\gamma_{GB}$ is the effective mobility, and k_1 is the rate constant. Although the effective grain boundary mobility can be easily determined for systems by direct and simple grain size measurements with time, the main drawback is that the mobility and the surface energy cannot be separated.

1.3 Alumina

1.3.1 α-Alumina Structure

Alpha-alumina (α-Al_2O_3) is typically known as the stable structure of alumina, although there exist various metastable structures for alumina. The α-alumina structure exhibits a rhombohedral (corundum) structure characterized by a space group of $R\bar{3}C$ (No. 167). When representing α-alumina, for simplicity, a hexagonal unit cell is commonly used. This unit cell contains 30 atoms in total: 12 aluminum atoms and 18 oxygen atoms (see

Figure 9). The lattice parameters for this hexagonal unit cell are a=b=0.4754nm, c=1.299nm, with α=β=90° and γ=120°.

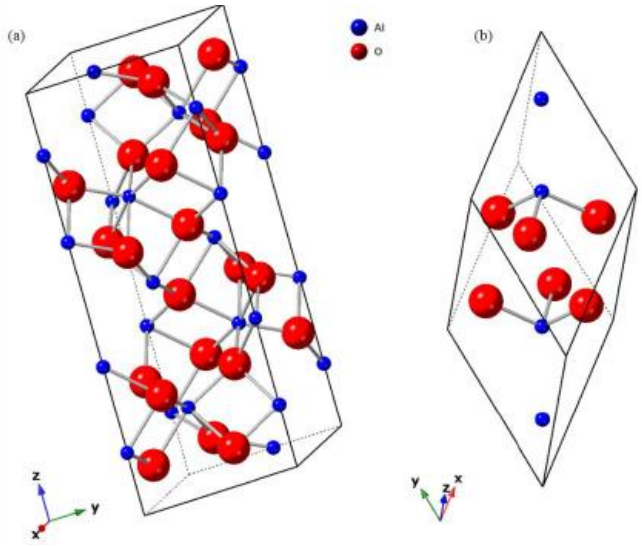

Figure 9: Schematic drawing of the hexagonal (a) and rhombohedral (b) unit cells of α-alumina. The blue spheres represent aluminum cations, and the red spheres represent oxygen anions [20].

α-alumina is commonly utilized as a crucial component in the manufacturing of advanced ceramics, refractories, and abrasive materials. In the field of ceramics, α-alumina is prized for its relatively high thermal conductivity, hardness, and wear resistance, making it useful for producing ceramic components for cutting tools, insulating materials, electronic substrates, armor, and in biomaterials. These applications and properties make α-alumina one of the most studied ceramics.

The equilibrium crystal shape (ECS) of alumina has been extensively studied through both experimental and theoretical approaches. These studies have identified that at 1600ºC, 1800ºC and in vacuum, for undoped and some doped alumina the following planes have the lowest energy [21-25] :basal (C-plane) (0001), rhombohedral (R-plane) $(\bar{1}012)$, prismatic (A-plane) $(11\bar{2}0)$, pyramidal (P-plane) $(11\bar{2}3)$, and structural rhombohedral (S-plane) $(1\bar{1}01)$, which are indicated in Figure 10.

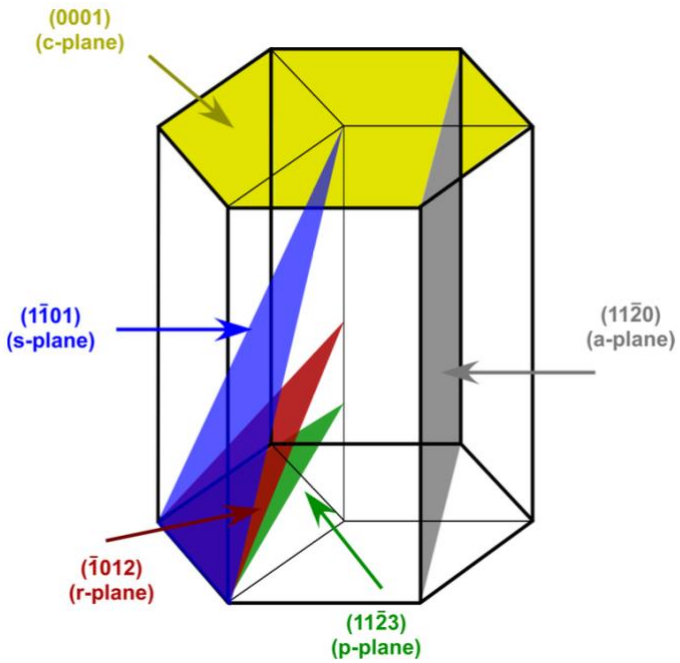

Figure 10: Schematic illustration of the crystallographic planes of alumina.

1.4 Grain Boundary Mobility in Alumina

1.4.1 Grain Boundary Mobility in MgO-Doped Alumina

Achieving full density and limiting grain growth was a challenge for undoped alumina, initially limiting its technological applications. The introduction of MgO as a dopant in alumina significantly advanced the materials densification process, as first demonstrated by Coble in the early 1960s. His work enabled the production of high-density, translucent alumina, particularly useful for applications like high-pressure sodium lamps [26]. The addition of Mg not only facilitated full densification but also played a crucial role in minimizing abnormal grain growth and reducing both grain boundary mobility and grain size, making it a standard practice in alumina manufacturing.

The solubility limit of MgO in alumina was previously reported by Roy and Coble to be 300 ppm for MgO in alumina at 1630°C; however, they did not measure the actual Mg concentration in the alumina after sintering [27].

Studies by Bennison and Harmer showed that doping high-purity alumina with 200 ppm of MgO resulted in a significant reduction in grain boundary mobility, from 1.74×10^{-19} m^3/sec in undoped alumina to 3.9×10^{-20} m^3/sec. This reduction led to a more uniform microstructure with smaller grains compared to undoped alumina [28].

Similarly, Rödel and Glaeser found that doping alumina with 250 ppm of MgO decreased the grain growth constant K_1 from 28.5×10^{-3} sec^{-1} to 7.1×10^{-3} sec^{-1}, resulting in almost fully dense materials with lower pore density, particularly at grain boundary junctions [29]. Both works reported a Mg content measured *before* sintering.

Miller et al. measured the solubility limit of MgO at 1600°C using quantitative wavelength dispersion spectroscopy (WDS) and found it to be 132 ± 11 ppm [30]. In a subsequent study, Akiva et al. examined the effects of Mg on the mobility of alumina at a concentration of Mg that was experimentally verified to be below the solubility limit [31]. Their results demonstrated a decrease in grain boundary mobility due to the solute drag effect.

1.4.2 Grain Boundary Mobility in Ca-Doped Alumina

Although the solute drag effect typically reduces grain boundary mobility, some experimental evidence suggests that some dopants or impurities present in concentrations below their solubility limit can actually enhance the mobility. Ca in alumina has been shown to increase grain growth and grain boundary mobility.

Bae and Baik, along with Jung and Baik, investigated how CaO affects abnormal grain growth in alumina [15, 32]. They reported a critical Ca concentration of around 30 ppm, which leads to abnormal grain growth, and linked this phenomenon to the formation of intergranular films with a minimum thickness of 0.35 nm and a composition resembling calcium hexaaluminate ($CaO \cdot 6Al_2O_3$). In their work they used ultrapure alumina powder (99.999%), and since the total Ca content was measured using inductively coupled plasma (ICP) spectroscopy, they acknowledged that the measured Ca concentration included contributions from both the alumina grains and the grain boundaries.

Altay and Gulgun focused on the influence of Ca on the alumina microstructure, where they found a grain boundary concentration of $\Gamma_{Ca} = 3$ atoms/nm^2, above which the grain morphology changed from equiaxed to elongated (Figure 11) [16]. In their work, they assumed a hypothetical Ca concentration at grain boundaries, assuming zero Ca in solution in the grains, and they did ***not*** measure the actual Ca content.

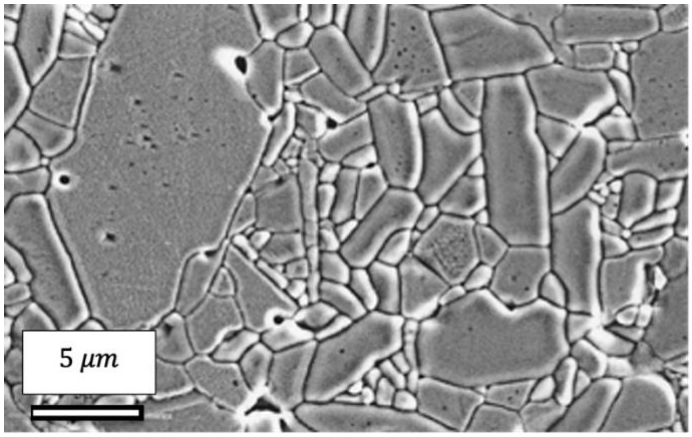

Figure 11: SEM micrograph showing abnormal and elongated growth in alumina doped with ~ 350 ppm Ca [16].

1.4.1 Complexions in Alumina

Complexions are equilibrium states of surfaces, characterized by a specific 2-D structure and chemical content. Grain boundary complexions are equilibrium interfacial states that exist at the grain boundaries in polycrystalline materials, believed to play a crucial role in the material's microstructural evolution and properties.

Complexions, as described by Dillon et al. are distinct thermodynamic phases, much like bulk phases, but confined to the grain boundaries (or surfaces) [33]. Complexions can vary in apparent width and chemical content, ranging from partial coverage of a single layer to atoms, to more complex multilayered or disordered structures, depending on factors such as temperature, pressure, and chemical composition.

Kaplan et al. further elaborated on the concept, explaining the influence of changes in complexions on wetting phenomena. They highlighted that complexions could influence critical processes such as grain growth, sintering, and mechanical behavior by altering the mobility of grain boundaries and the interaction between grains [34].

Dillon and Harmer related grain boundary complexions to the increased grain boundary mobility in Ca-doped and Si-doped alumina. They observed an enhanced grain boundary mobility in Ca-doped alumina, and attributed this increase to a complexion transition, where each distinct complexion exhibits different mobilities (Figure 12). They proposed that the mobility variations are linked to the amount of excess Ca at the grain boundary, which alters its chemistry and structure. However, it is important to note that they did

not directly correlate grain boundary mobility with the specific chemistry of the boundaries but instead with the apparent width of the grain boundaries as observed through microscopy. The bulk chemical content associated with the mobilities was actually the target concentration when dopants were added to the powders, and not the actual concentration after the sintering process [12].

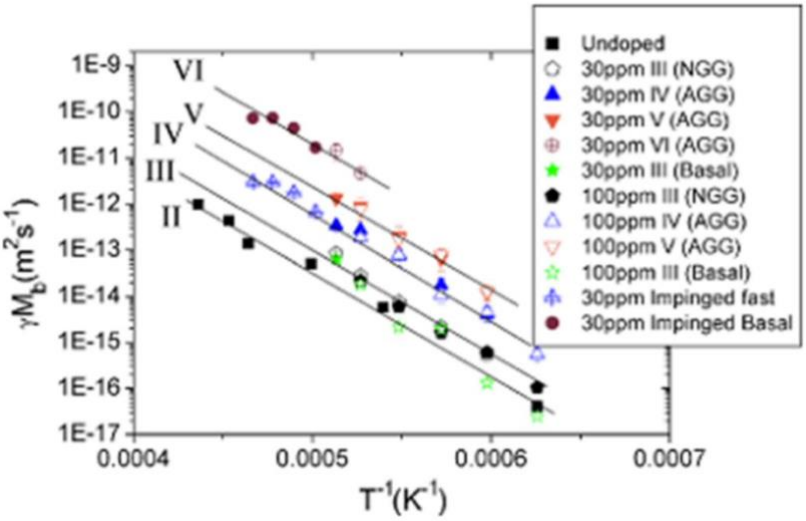

Figure 12: Grain boundary mobilities for different complexions in normal and abnormal grains in Ca-doped alumina [12].

1.4.2 Single Crystal Growth into Ca-doped Alumina

Akiva et al. measured the effective mobility of the basal (0001) plane growing into polycrystalline alumina [31]. The measurements were done by diffusion bonding fully dense polycrystalline undoped, Mg-doped (23 ppm), and Ca-doped (13 ppm) alumina to (0001) oriented sapphire wafers. The dopants concentration was well below their solubility limit at 1600°C; 32 ppm for Mg, and 51 ppm for Ca [14,30].

The effective mobilities were estimated by measuring the displacement of the single crystal in time at 1600°C. It was found that the mobility of the (0001) plane decreased to 1.1×10^{-15} m²/s in Mg-doped alumina, compared to 2.5×10^{-15} m²/s in undoped alumina, but increased to 3.2×10^{-15} m²/s in Ca-doped alumina.

In the same work, an excess of 2.6 Ca atoms/nm^2 was measured at the boundary between the (0001) single crystal and the Ca-doped polycrystalline alumina, using energy dispersive spectroscopy (EDS) in a scanning transmission electron microscope (STEM). While this excess was correlated to the increased mobility of the basal (0001) plane, it did not explain the elongated plate-like grain morphology.

1.5 Equilibrium Crystal Shape

1.5.1 Surface Energy and Wulff Construction

1.5.1.1 Surface energy

Surface energy (γ) refers to the energy required to increase the surface area of a material by one unit, while keeping conditions like temperature, volume, and chemical potential constant. This means that atoms at the surface of a material will have higher energy than those in the bulk because they have more free bonds (or undersaturated bonds). As a result, materials tend to adopt a shape that minimizes their surface energy to reach equilibrium, which lowers the total energy.

In materials where the surface energy is isotropic, the material tends to form a shape that minimizes the surface area for a given volume; typically, a sphere, as seen in liquids. However, in most polycrystalline materials, surface energy is anisotropic and varies with crystallographic orientation. This anisotropy arises from differences in atomic bonding, the spacing between atomic planes, charge distribution, and the ability of the surfaces to go through reconstruction and or/ relaxation to reduce energy. Consequently, the equilibrium shape of a solid will reflect these anisotropies, resulting in more complex geometries than those found in isotropic materials.

1.5.1.2 The γ Plot

The surface energy versus the crystallographic orientation is represented by two-dimensional or three-dimensional plot, called the γ-plot. The γ-plot is typically presented in polar coordinates, where each point on the plot corresponds to a specific crystallographic plane, and the distance from the center of the plot to the point represents the surface energy associated with that plane as shown in Figure 13.

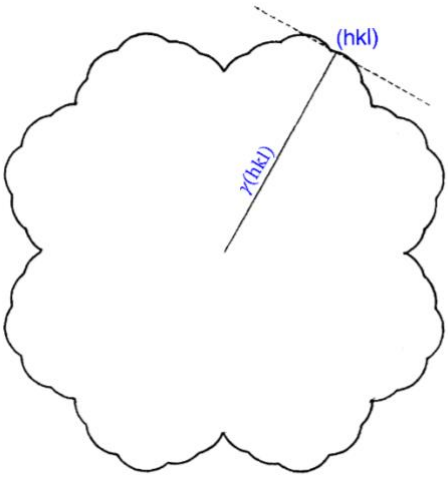

Figure 13: Typical polar plot of a crystal surface, (reproduced from [35]).

The extent of surface anisotropy in the material can vary based on factors such as temperature, chemical composition, and crystallographic orientation. The relationship between surface energy and these actors is explained by the Gibbs adsorption equation [36]:

$$d\gamma(n) = -S(n)dT - \sum_{i=1}^{n} \Gamma_i d\mu_i \qquad (13)$$

where *n* is a unit vector normal to the surface, *S(n)* is the surface entropy, *T* is the absolute temperature, Γ_i is the surface excess of solute species *i*, and μ_i is the chemical potential of species *i*.

The chemical potential of the surface is an important factor affecting the surface energy, and the Gibbs adsorption equation shows that this chemical potential is changing as a function of interfacial adsorption or impurity segregation, and as a result, decreasing the surface energy.

1.5.1.3 Wulff Construction

A crystal with anisotropic surface energy will adopt an equilibrium shape to minimize its total energy. This equilibrium shape, known as the Wulff shape or equilibrium crystal shape (ECS), represents the geometric configuration that minimizes the total surface energy for a fixed volume. The Wulff construction provides a geometric method for predicting the crystal shape when the surface energy, γ, is known for all orientations.

In this process, a γ-plot is used, and planes are drawn perpendicular to the radius vectors extending from the center to each point on the plot. The Wulff shape is defined by the inner envelope formed by these planes [37] (see Figure 14). The facets in the Wulff shape correspond to low-energy planes, typically located at cusps in the γ-plot. The resulting shape can be entirely faceted or may include both flat facets and curved surfaces, depending on the degree of surface energy anisotropy.

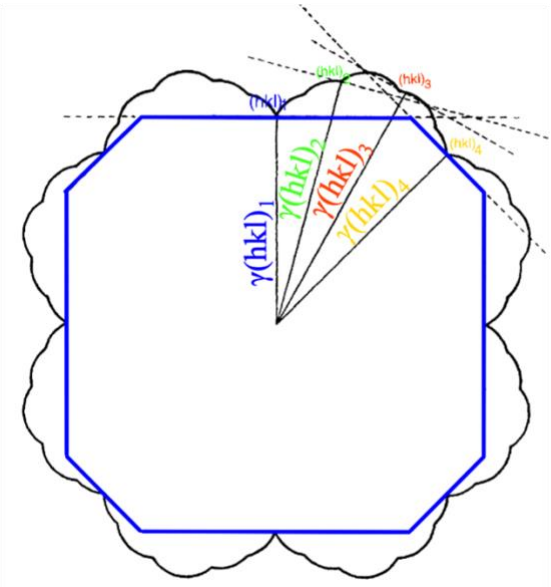

Figure 14: Wulff shape constructed using γ-plot, (reproduced from [35]).

For a crystal in equilibrium, the distance from the center of the crystal to any facet in a given direction is proportional to the surface energy of that facet. This relationship can be expressed as:

$$\frac{\gamma_1}{l_1} = \frac{\gamma_2}{l_2} = \cdots = \frac{\gamma_i}{l_i} = const \qquad (14)$$

where γ_i is the surface energy of the *i*th facet/plane, and l_i is the distance from the center of the ECS to the center of the facet/plane *i* (along its normal vector). This method has been used to determine relative surface energies in metals and ceramics by analyzing small particles and pores. However, it only allows for the calculation of relative surface energies. To determine absolute surface energies, at least one absolute energy value would be required.

1.5.2 The Equilibrium Crystal Shape of Undoped Alumina

The Wulff construction has been employed to investigate the ECS of undoped alumina in two notable studies. Choi et al. studied internal cavities in sapphire single crystals, annealed at 1800°C and 1600°C [22]. The cavities were formed by indentation and the shape and size of the annealed cavities were studied by TEM from a few specific orientations to retrieve information about the faceted shape as a function of the specimen orientation. For example, Figure 15 (a) and (b) present two different cavities in *A*-oriented sapphire single crystal.

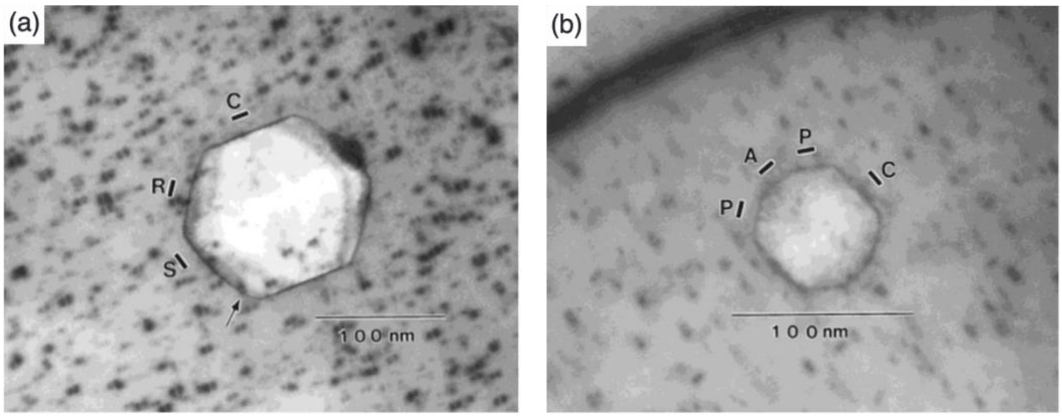

Figure 15: TEM micrographs of two different cavities in an *A*- oriented specimen annealed at 1600C for 50 h in air. The zone axes are (a) $[2\bar{1}\bar{1}0]$, (b) $[10\bar{1}0]$ [22].

The relative surface energies were estimated by measuring the distances between the facets, relative to the distance between the *C*-facet planes (the basal planes). The surface energies for these planes relative to the surface energy of the basal plane were γ_R =1.05, $\gamma_A = 1.12$, $\gamma_P = 1.06$ and $\gamma_S = 1.07$ (planes and indexes mentioned in section 1.3.1- Figure 10).

The ECS of undoped alumina simulated using the relative surface energies measured is presented in Figure 16.

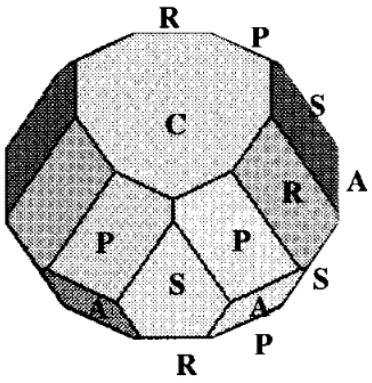

Figure 16: Simulated cavity shape using anisotropic surface energy [22].

In a different work, Kitayama et al. studied internal pores fabricated in polycrystalline undoped alumina using lithography, diffusion bonded to sapphire single crystal and annealed at 1600°C [25]. The faceted pores were exposed by mechanical polishing and observed using scanning electron microscopy (SEM) (see Figure 17).

The facet-to-facet distances were measured, in a similar way to Choi et al., from which the relative surface energies, relative to the *C*-facet plane, were estimated. Consistent with Choi et al., the same five planes: *C, A, R, P* and *S,* were observed, and the relative surface energies were γ_R =0.855, $\gamma_A = 0.974$, $\gamma_P = 0.957$ and $\gamma_S = 0.947$.

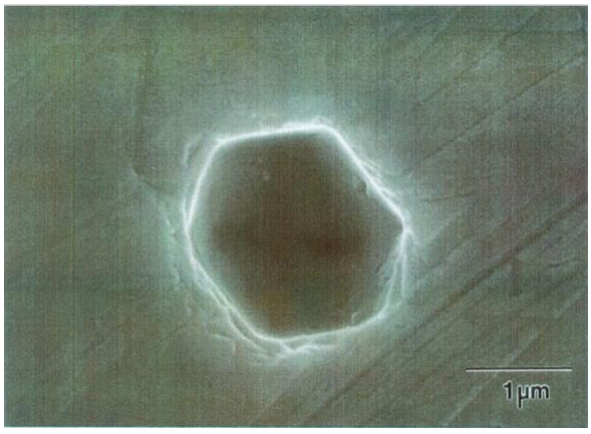

Figure 17: SEM micrograph of a pore exposed parallel to the *A*-plane after 480 h at 1600°C [25].

The relative energy values show disagreement between the two studies, where in the first one, the *C*-plane was found to have the lowest energy, and in the second one, the *R* plane had the lowest surface energy. This difference can be attributed to the experimental

procedures used by each group, where polycrystalline alumina, used by Kitayama et al., tends to have higher level of impurities than single crystal sapphire (used by Choi et al.).

1.5.3 Ca Segregation to Grain Boundaries

Segregation at grain boundaries or surfaces can significantly alter surface energy by changing the chemical potential as explained in 1.5.1.2, thereby influencing the ECS by modifying the relative stability of different crystallographic planes.

It was shown in previous works that Ca segregates to grain boundaries in Ca-doped alumina, although the actual Ca content at the grain boundaries was not measured [12,15,16,32].

Akiva et al. studied Ca-doped alumina at a concertation below solubility limit, using EDS in a STEM, and measured an excess of 2.6 Ca atoms/nm^2 (detection limit of 1.3 Ca atoms/nm^2), proving equilibrium (Gibbisian) segregation of Ca to the grain boundaries, where this excess was correlated to the increased GB mobility in alumina [14]. It is also expected that the Ca excess would have an influence on the ECS of Ca doped alumina.

2. Research Goals

The primary goal of this research is to measure the anisotropic grain boundary mobility of Ca-doped alumina, in order to understand if the elongated grain shape seen in Ca-doped alumina is due to kinetic (grain boundary mobility) effects.

By studying the behavior of Ca at the grain boundaries, this research aims to elucidate the mechanisms through which it alters both the grain boundary mobility and the anisotropic growth of alumina grains, offering insights into its broader impact on material properties.

3. Experimental Methods

3.1 Sample Preparation

3.1.1 Undoped and Ca-Doped Polycrystalline Alumina

To produce high-purity polycrystalline alumina samples, 150 g of α-Al_2O_3 powder (99.99% purity, Ceralox HPA 0.5, Tucson, AZ) was dispersed in 100 g of distilled water. For the Ca-doped polycrystalline alumina samples, 300 g of the same high-purity α-Al_2O_3 powder was mixed with calcium nitrate ($Ca(NO_3)_2 \cdot 4H_2O$, Carlo Erba Reagents, Milan, Italy) and dispersed in 150 g of distilled water.

The alumina suspensions were deflocculated by adjusting the pH to approximately 4 through the addition of analytically pure HCl. This pH adjustment optimized the dispersion of the alumina particles within the slurry. The suspensions were then mixed continuously for 24 h using a ball-milling system without milling balls to minimize contamination, following the findings of Miller et al., which showed that using ZrO_2 milling balls could introduce up to 50 ppm of zirconium into alumina grains [30].

After mixing, green bodies were formed by vacuum filtration and air-dried at room temperature for 24 h, followed by further drying at 100°C for 5 h. The green bodies were then sintered in air at 1600°C for 2 h (heating rate ~ 15 °C/min) resulting in dense alumina samples with a relative density exceeding 95%.

To further process the samples, bulk pieces from the sintered slips were annealed in air at 1600°C for periods of 2, 4, 6, 8, and 10 h (heating rate ~ 15 °C/min). After annealing, cross-sectional samples were mechanically polished using a diamond suspension on polishing cloths, starting with a diamond size of 125 µm and finishing with a 0.25 µm diamond size for final polishing.

For grain size measurements, thermal etching to induce grain boundary grooving was conducted in an air furnace at 1250°C for 2 h.

3.1.2 Diffusion Bonding

Well-polished cross-sectional samples from the polycrystalline undoped and Ca-doped alumina (prepared as explained in 3.1) were calcined at 800°C for 2 h to remove any residual moisture, impurities, and organic substances from polishing, ensuring that the surfaces were clean.

Sapphire substrates were placed between polycrystalline alumina samples, and a pressure was applied via a static weight of 900 gr (of sintered alumina), as illustrated in Figure 18, and annealed in air at 1600°C for 48 h

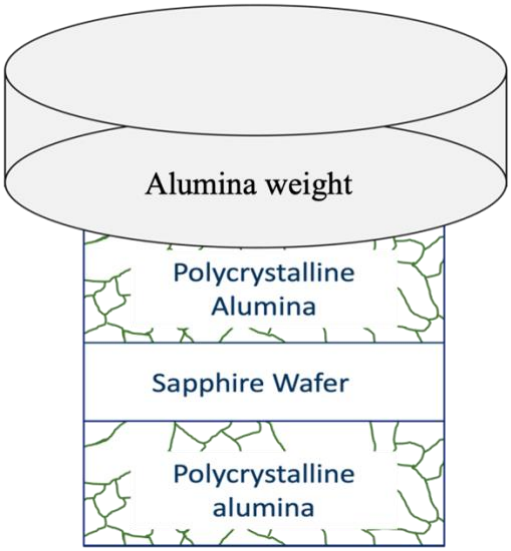

Figure 18: Schematic illustration of the diffusion bonding experimental configuration.

Two sets of diffusion-bonded samples were prepared: one with undoped polycrystalline alumina bonded to *C*-, *A*-, and *R*-oriented sapphire, and another with Ca-doped polycrystalline alumina bonded to *C*-, *A*-, and *R*-oriented sapphire. The bonded samples were annealed in air at 1600°C for 20, 30, 40, and 50 h. After annealing, each sample was sectioned, and the interior was mechanically polished using a diamond suspension on polishing cloths, starting from a diamond size of 75 µm and concluding with a diamond size of 0.25 µm.

3.1.3 Focused Ion Beam – Fabrication of Holes and Needles

Xenon focused ion beam (FIB) (Thermo Fisher Helios 5 Plasma FIB) microscopy was utilized to fabricate holes and needles in polycrystalline alumina for subsequent ECS

analysis. To prevent sample charging and to achieve sharp, well-defined holes and needles, the samples were coated with a conductive carbon layer prior to FIB processing. The hole fabrication process was conducted at an accelerating voltage of 30 kV with an ion current of 10 pA, resulting in 800 nm diameter holes and 1 µm in depth.

To fabricate needles in the polycrystalline grains, round holes with inner radius of 3 µm, and an outer radius of 6 µm where initially milled, at an accelerating voltage of 30 kV with an ion current of 1 nA, followed by finer milling at lower ion current (0.1 nA).

3.2 Characterization Methods

3.2.1 Density

The density of specimens (ρ_{spec}) was determined using the Archimedes‘ method following ASTM standard c 20-92:

$$\rho_{spec} = \frac{\left(\frac{D}{W-S}\right)}{\rho_{alumina}} \tag{15}$$

where D is the dry weight, W is the saturated weight, S is the suspended weight of the sample, and $\rho_{alumina}$ is the theoretical density of alumina (3.97 gr/cm^3).

3.2.2 Wavelength Dispersive Spectroscopy

The dopants and impurities concentrations were measured using WDS (Oxford Instruments, High Wycombe,U.K.) mounted on a scanning electron microscope (ThermoFisher Prisma E-SEM).

WDS measurements were acquired at a working distance of 10 mm, a magnification of x15,000, a spot size of 8.7 resulting in a probe current of at least ~40 nA, and a measurement time of 20 sec. An accelerating voltage of 25 kV was used to optimize between high signal intensity and low background intensity. The background intensity in the peak position was calculated by linear interpolation. More than 30 measurements were taken from random locations in the sample for each element.

A polyethylene terephthalate (PET) crystal was used as a monochromator for the measurements of Ca and Si, and a thallium acid phthalate (TAP) crystal for the measurements of Mg. Diopside $CaMg(Si_2O_6)$ was used as a standard for Mg, Ca and Si quantification.

The dopant's concentration was calculated according to:

$$C = k \cdot C_{std} \cdot g_{ZAF} \tag{16}$$

where C_{std} is the concentration within the diopside standard (C_{std}=1 for pure elements), $k = \frac{I_{sample}}{I_{std}}$ is the ratio between the measured intensities of the peaks between the unknown sample (I_{sample}) and the standard (I_{std}), and g_{ZAF} is the ZAF correction factor where Z is for atomic number correction, A for adsorption correction and F for florescence correction. The ZAF correction factor was calculated using XPHI software [38].

The element of interest was detected in each sample under the condition that the intensity (I) measured is larger the intensity of the background (I_{bgd}), ($I > I_{bgd}$), is fulfilled at a level of confidence of probability (P) according to:

$$I - I_{bgd} \geq t(P, f) \cdot \sqrt{2} \cdot \sigma_{bgd} \tag{17}$$

where $t(P, f)$ is a coefficient for the confidence probability P and a number of degrees of freedom (f) ,$f = m - 1$, for m number of measurements, and σ_{bgd} is the standard deviation of the background intensity. For a background intensity with a Poisson distribution, the limit of detection with a confidence probability of 97.5% is:

$$C_{limit,0.975} = C_{std} \cdot g_{ZAF} \cdot \frac{2\sqrt{2I_{bgd}}}{\sqrt{m\tau}I_{std}} \tag{18}$$

where τ is the single measurement time.

3.2.3 Scanning Electron Microscopy

Scanning electron microscopy (SEM) was used for microstructure characterization on polished cross-sectioned samples, which was conducted using the Zeiss Ultra-Plus field emission gun SEM (Oberkochen, Germany). The micrographs were obtained using an Everhart Thornley detector at working distances between 3-5 mm, and an accelerating voltage of 1.5 KeV.

3.2.4 Grain Size Analysis

Grain sizes were measured using the linear intercept method [39], from more than 700 grains in each cross-sectional sample, from 10 different SEM micrographs. A correction factor of 1.56 was used to correlate between the average grain size ($\bar{G}$) , and the average intercept length ($\bar{L}$), thus $\bar{G} = 1.56\,\bar{L}$.

Grain growth was characterized using a parabolic behavior in equation 12 (section 1.2.51.2.5) from which the effective mobilities of the polycrystalline samples were estimated.

$$\bar{G}_t^{\,2} - \bar{G}_0^{\,2} = 4M_{GB}\gamma_{GB}t = k_1 t \tag{12}$$

3.2.4.1 Surface vs. Bulk Grain Size Measurements

One of the challenges in determining the effective grain boundary mobility using Equation 12; is measuring the grain size close to the surface. During this research, grain size measurements from bulk pieces near the outer surface of the sintered slip did not show significant grain growth with time at 1600°C. This is not a trivial issue, as there are reports in the literature of grain growth measurements where the authors bypassed the tedious tasks of sectioning and polishing; instead measuring the grain size directly from the surface of the sintered bodies.

In order to understand the surface effect, two sets of measurements were done on Ca doped bulk pieces. The first set of measurements was from the surface, which was done by polishing and thermally etching the surface of the bulk pieces before annealing, each polished sample was then annealed for 2, 4, 6, 8 and 10 hr at 1600°C, and grain size

measurements were done from the annealed surface. The second set was from cross-sectional samples from the center of the annealed samples, which were polished and thermally etched after the annealing process and then grain size measurements were conducted.

3.2.5 Measuring the Effective Mobility of Single Crystal Sapphire

The growth rate of the single crystal sapphire wafers was measured as it grew at the expense of grains in the polycrystalline sample. This was achieved by determining the position of the sapphire wafer after annealing compared to its initial position, by tracking the position of occluded pores.

The driving force for growth of the sapphire wafer is defined by the grain size of the polycrystalline alumina to which it was bonded:

$$\frac{d(\overline{\Delta L})}{dt} = \frac{\gamma_{GB} M_s}{G_t} = \frac{\gamma_{GB} M_s}{\sqrt{k_1 t + \overline{G_0}^2}} \tag{19}$$

where ΔL is the average displacement of the sapphire wafer at time t, and M_s is the mobility of a single crystal (sapphire wafer).
Integrating Equation (19) results in:

$$\overline{\Delta L}(t) = \gamma_{GB} M_s \frac{\sqrt{k_1 t + \overline{G_0}^2} - \overline{G_0}}{k_1} \tag{20}$$

Taking the squared form of the equation, gives the linear relation with time:

$$\overline{\Delta L^2}(t) = \left(\frac{2\gamma_{GB} M_s}{k_1}\right)^2 \left(\sqrt{k_1 t + \overline{G_0}^2} - \overline{G_0}^2\right)^2 = \frac{4\,{\gamma_{GB}}^2 {M_s}^2}{k_1} t + const \tag{21}$$

The effective single-crystal mobility ($\gamma_{GB} M_s$) can be estmiated from the slope of the squared displacement as a function of time.

3.2.6 Time to Reach Equilibrium

The time required to reach equilibrium was estimated by fabricating holes with specific radius and depth in polycrystalline Ca-doped alumina grains. The holes were annealed for different periods of time at 1600℃, and the lengths of two edge-on facets (L_A and L_B) was measured after each annealing process.

The ratio $\frac{L_A}{L_B}$ was measured as a function of time, and the time required to reach equilibrium was estimated as the time at which Equation (22) is fulfilled:

$$\frac{L_A}{L_B} = const \tag{22}$$

3.2.7 Electron Back-Scattered Diffraction

Electron backscattered diffraction (EBSD) mapping was conducted on well-polished cross-sectional samples, in order to determine the orientation of the polycrystalline grains in undoped and Ca-doped alumina. EBSD analyses were conducted using in-lens energy selected back scattered detector (imaging) mounted on Zeiss Ultra-Plus field emission gun SEM, with a working distance of 16–18 mm, an accelerating voltage of 20 keV, and a sample tilt angle of 70 degrees for optimal diffraction pattern acquisition. The diffractions were analyzed using ESPRIT BRUKER software.

Orientations acquired from EBSD were used to identify the planes of the facets in annealed holes (fabricated in section 3.1.3) by simple angle measurements and comparison with the ECS of undoped alumina (1.5.2).

3.2.8 Focused Ion Beam Cross-Sectioning

Fully faceted annealed holes were cross-sectioned in a selected direction using ion milling in a Xenon FIB. The samples were tilted at 52 degrees, and the holes were coated with a 1 µm carbon layer to provide protection, prevent charging, and ensure clean, straight cross-sections. Initial milling was performed at 30 keV with an ion current of 4 nA to a depth of 10 µm, exposing a near-hole region and allowing imaging of the interior.

Further milling of hole itself to obtain a cross-section through the center was done using the same accelerating voltage, with an ion current of 1 pA and a depth of 20 µm.

4. Results

4.1 Dopant and Impurities Content

Since our interest is to understand the influence of Ca on microstructural evolution below its solubility limit, it is crucial to make sure that its content is indeed below the solubility limit after sintering the samples, since dopants added to the powder or in solution may evaporate during sintering, altering the expected concentration. Also, determining the precise levels of other dopants and impurities in the samples, especially Mg and Si, which are known to be common dopants/ impurities in our working environment, is critical for evaluating their impact on grain growth. Impurities can be introduced during processing from the starting powder, molds, furnaces, and other lab equipment.

To measure the actual concentration of an element in a meaningful way, the minimum concentration that can be detected had to be determined. This was measured for each specific sample, considering the WDS/SEM operating conditions and the number of measurements performed, using Equation (18).

The detection limits for Ca, Si and Mg and their actual content in the sintered samples are presented in Table 1.

Table 1: Summary of the dopant/impurity concentrations in the samples produced for this study.

Sample	Dopant	Concentration [ppm]	Detection limit [ppm]
Undoped alumina	Ca	4 ± 1	3
	Mg	< Detection Limit	5
	Si	< Detection Limit	17
Ca-doped alumina	Ca	15 ± 1	2
	Mg	9 ± 2	7
	Si	14 ± 1	10

The solubility limit of Ca, Mg and Si in alumina at 1600°C is 51 ppm, 132 ppm and 188 ppm, respectively [14,30,40]. These measurements confirm that the Ca content is below its solubility limit in Ca doped alumina, and that Si and Mg are present at low concentrations (and well below their solubility limit).

4.2 Density and Microstructure

4.2.1 Undoped Alumina

The relative density of the undoped alumina was measured to be 98%, and the microstructure of undoped alumina, annealed in air at 1600°C for 0 h and for 8 h, is presented in Figure 19. From the microstructure, it can be seen that the samples are dense, as stated, where the faceted pores seen in the micrographs are grain pull-outs that occur during polishing. The micrographs also show equiaxed grain growth, and no abnormal growth or elongated grains (for all annealing durations).

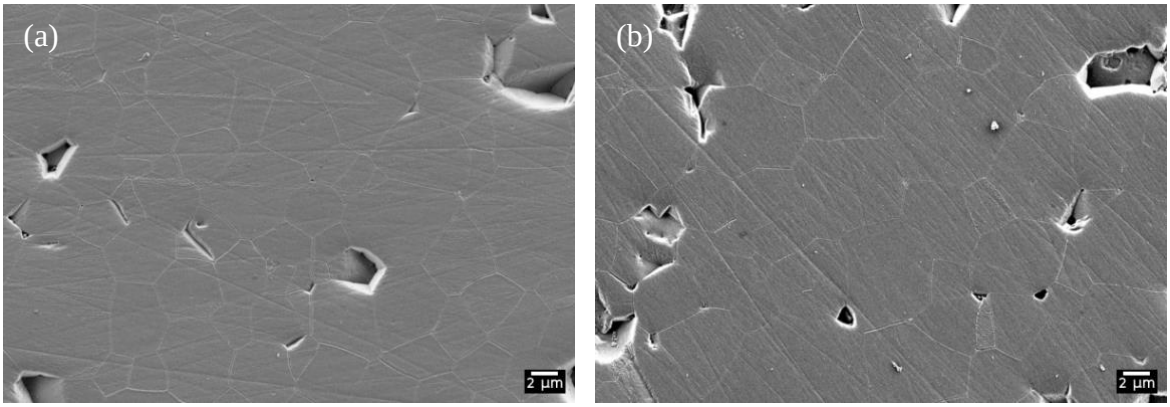

Figure 19: Secondary electron (SE) SEM micrographs (polished and thermally etched cross-sections) of undoped alumina microstructure annealed in air at 1600°C for (a) 0 h, and (b) 8 h.

4.2.2 Ca-Doped Alumina

For the Ca-doped alumina, the relative density was measured to be 97%. Figure 20 presents the microstructure of Ca-doped alumina annealed in air at 1600°C for 0 h and for 4 h, showing dense samples with equiaxed grains after relatively short annealing times (up to 4 h).

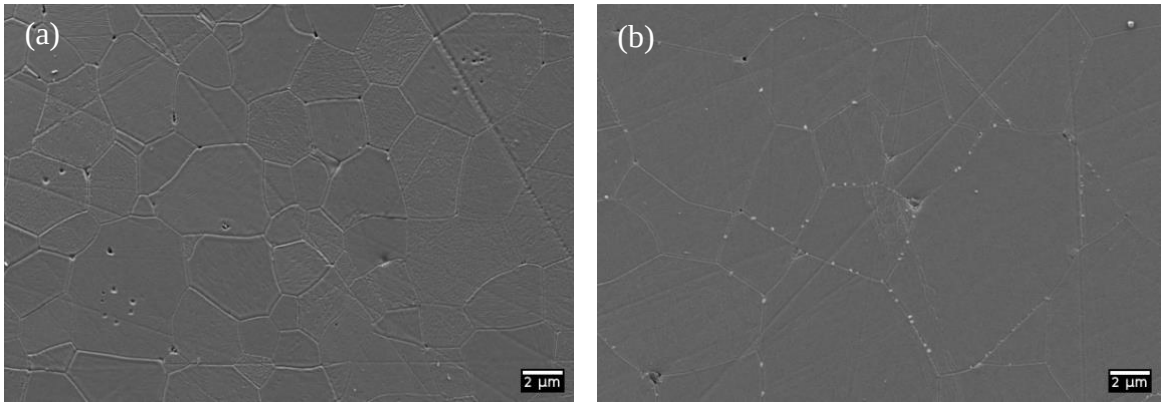

Figure 20: SE SEM micrographs (polished cross-sections) of Ca-doped alumina microstructure, annealed in air at 1600°C for (a) 0 h, and (b) 4 h. In (b) the small (alumina) particles at the grain boundaries are from the thermal annealing process.

Figure 21 presents the microstructure of Ca-doped alumina annealed for longer durations, 8 h and 10 h at 1600°C, where elongated grains are observed in the dense samples.

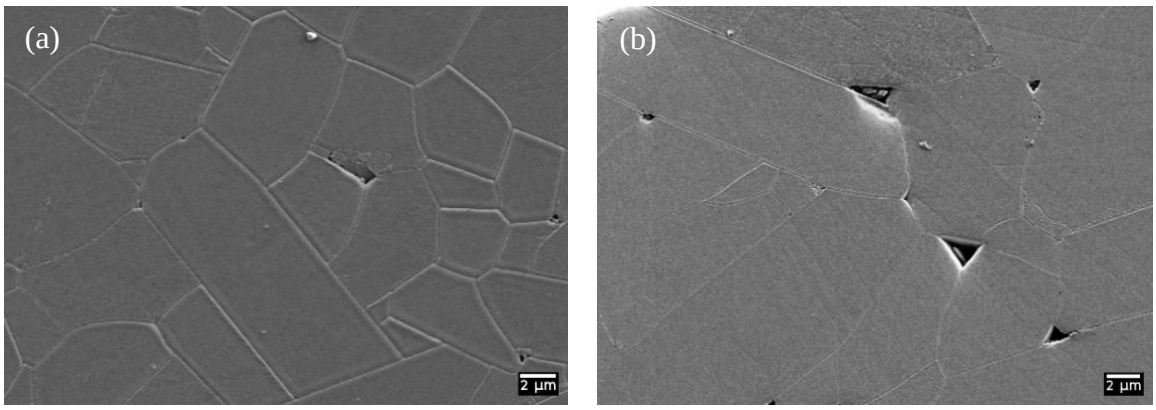

Figure 21: SE SEM micrographs (polished cross-sections) of Ca-doped alumina microstructure, annealed in air at 1600°C for (a) 8 h, and (b) 10 h.

The microstructure presented in the micrographs confirms that there is no observable effect on the microstructure due to the presence of the small amount of Mg and Si detected in the samples by WDS measurements, while the addition of 15 ppm of Ca results in elongated grain growth after extended (8 h, 10 h) annealing at 1600°C.

4.3 Effective Grain Boundary Mobility of Alumina at 1600ºC

In order to confirm the increase in the grain boundary mobility for the amount of Ca detected in WDS (15 ppm) in the Ca-doped polycrystalline alumina, the effective grain

boundary mobility was determined by measuring the change in grain size as a function of time at 1600°C.

The grain growth kinetics of undoped and Ca-doped polycrystalline alumina samples annealed at 1600°C in air are described in Figure 22.

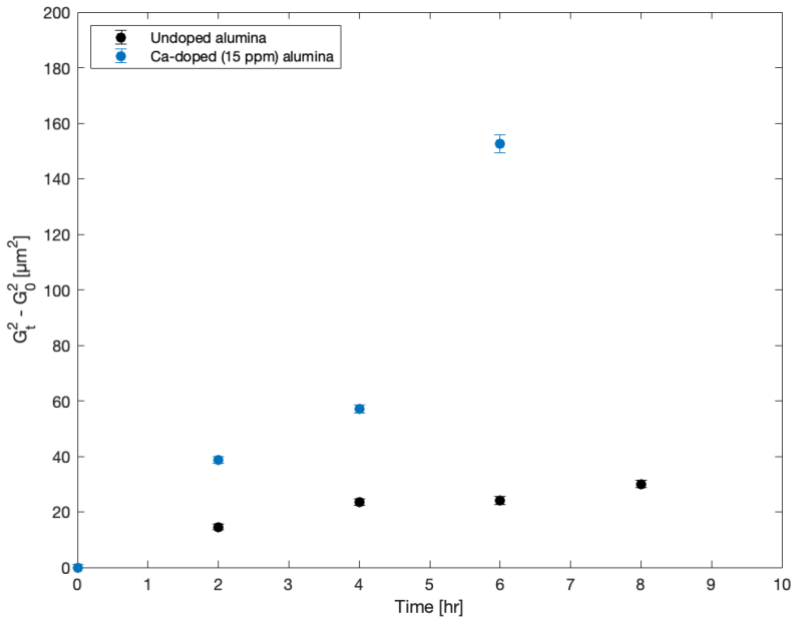

Figure 22: Grain growth kinetics of *undoped* alumina and, 15 ppm *Ca-doped* alumina samples annealed at 1600°C in air. The slopes represent the values of the effective mobility of the different samples, and the error bars represent the standard error.

The effective grain boundary mobility was determined from the parabolic grain growth kinetics, and for the Ca-doped samples it was determined from the early stages of growth (0, 2, 4 and 6 h of annealing at 1600°C), at which equiaxed grain growth was observed. For annealing times longer than 6 h elongated grains were observed and thus these grain sizes were not included in the mobility analysis.

The effective grain boundary mobility in the polycrystalline undoped alumina was measured to be 2.9 (± 0.4) $\cdot 10^{-16}$ m^2/sec, and 15 (± 2) $\cdot 10^{-16}$ m^2/sec in polycrystalline Ca-doped alumina, confirming the increase in the effective grain boundary mobility as a result of Ca doping at a content below solubility limit.

4.3.1 Morphology and Effective Grain Boundary Mobility Measured from the Bulk vs. from the Surface

Grain size measurements from the surface and from the bulk of annealed Ca doped alumina samples were done as explained in 3.2.4.1. The observed morphology is presented in Figure 23, where Figure 23 (a)-(c) show equiaxed grains on the surface after all annealing durations, while Figure 23 (d)-(f) show that elongated grains are observed after longer annealing times, as was seen in the previous section for the same Ca content.

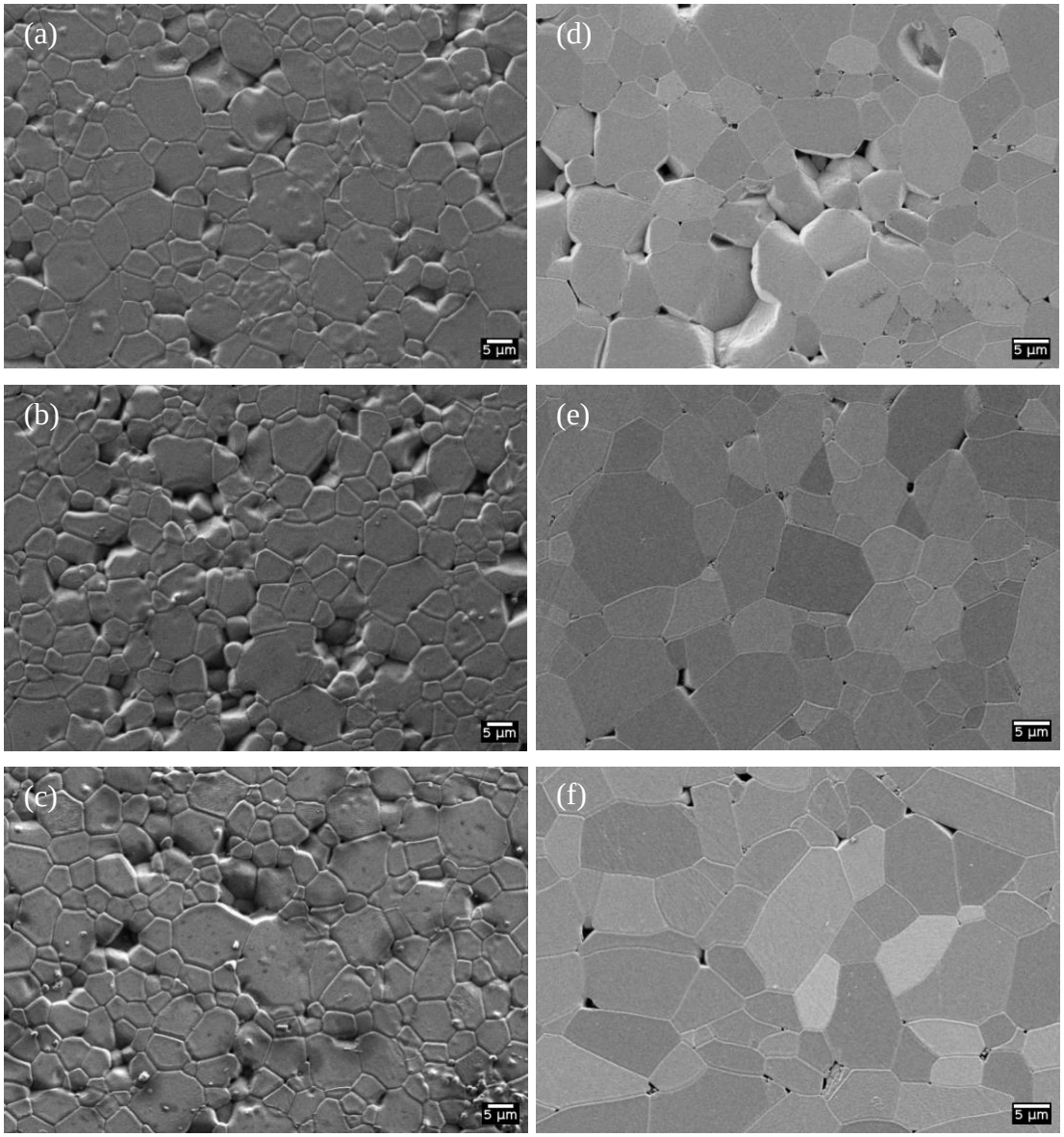

Figure 23: SE SEM micrographs (polished cross-sections) of Ca-doped alumina, annealed in air at 1600°C. (a)-(c) present the microstructure of the surface, after 2, 4 and 10 hr of

annealing, respectively. (d)-(f) present the microstructure of the bulk after 2, 4 and 10 hr of annealing, respectively.

The grain growth kinetics from the measured grain size are presented in Figure 24,where grain size measurements from bulk samples annealed for 8 and 10 hr were excluded due to the appearance of elongated grains.

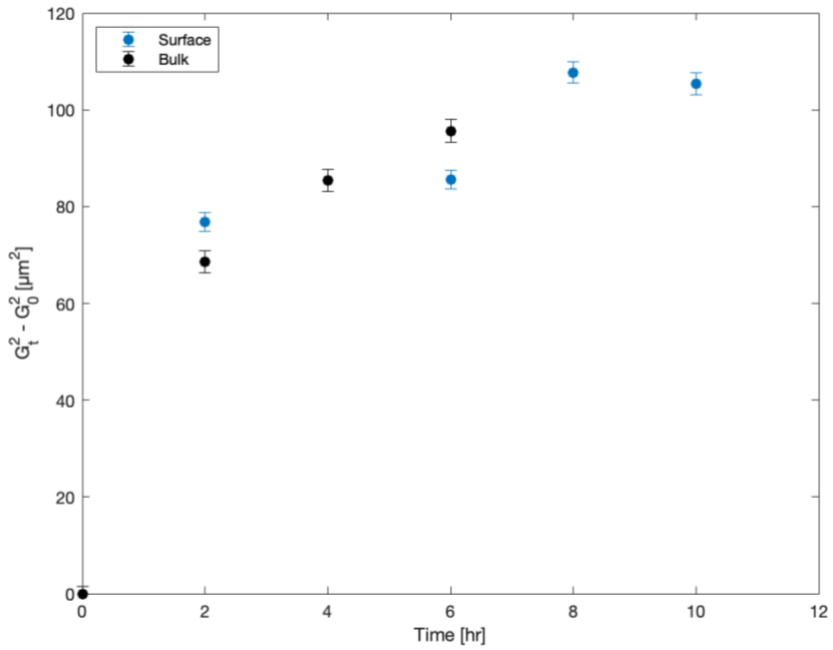

Figure 24: Grain growth kinetics of Ca-doped alumina samples annealed at 1600°C in air, measured from the surface and from the bulk. The slopes represent the values of the effective mobility of the different area of measurement.

The effective grain boundary mobility measured from the surface of Ca-doped polycrystalline alumina is 8.7 (± 1.4) $\cdot 10^{-16}$ m^2/sec, while the effective grain boundary mobility measured from the bulk is 13 (± 2.5) $\cdot 10^{-16}$ m^2/sec.

The effective grain boundary mobility measured from grain growth in the bulk; 13 (± 2.5) $\cdot 10^{-16}$ m^2/sec, is close to the effective grain boundary mobility measured in section 4.3 (15 (± 2) $\cdot 10^{-16}$ m^2/sec), for the same amount of Ca. However the effective mobility measured from the surface is significantly lower. This result shows an important effect of surface properties on grain growth.

The different morphology and different grain boundary mobility observed for bulk versus surface regions, could suggest different behavior of the grain boundary motion on the surface compared with the bulk. As was observed earlier, Ca segregates to the

grain boundaries significantly increasing the grain boundary mobility. The difference in the observed results suggests either a gradient of Ca concentration, increasing towards the center of the bulk, and thus the mobility is higher in the bulk, or that the same amount of Ca is present at the surface and in the bulk, but the grain boundary motion is affected (hindered) by other surface parameters (such as grain boundary grooves).

4.4 Anisotropic Grain Boundary Mobility of Alumina at 1600ºC

The growth of *C*-, *A*- and *R*- oriented single crystal wafers, diffusion bonded to polycrystalline undoped, and Ca-doped alumina, was measured by tracking the displacement of the grain boundary compared to detached pores at the interface, as a function of time at 1600℃.

Figure 25 presents an example of the displacement (ΔL) measured from *C*-oriented single crystal diffusion bonded to Ca-doped alumina, and annealed for 50 h at 1600℃, and from *A*-oriented single crystal diffusion bonded to undoped alumina and annealed for 20 h at 1600℃.

The growth of the *C* and *R*-oriented single crystals into the Ca-doped polycrystalline alumina was flat and more uniform than the growth of *A*-oriented, which showed a "wavy" and non-flat morphology at the interface. For the undoped alumina, only the *C* oriented single crystal preserved a flat morphology at the interface, while the *A* and *R* oriented were "wavy" and non-flat.

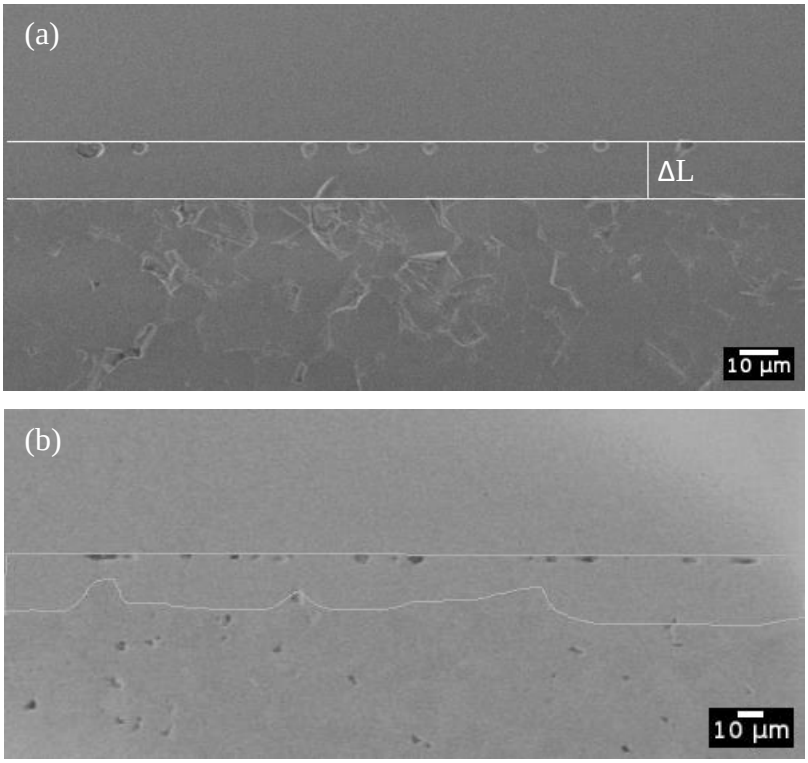

Figure 25: SE SEM micrographs of displacement of (a) *C* – oriented sapphire diffusion bonded to *Ca-doped* alumina at 1600°C for 50 h, and (b) *A* – oriented sapphire diffusion bonded to *undoped* alumina at 1600°C for 20 h. The interface between the single crystal and polycrystalline material is indicated by a white line, where the original interface (before crystal growth) is delimited by residual pores.

The measured squared displacements of the single crystals into undoped and Ca-doped polycrystalline alumina, as a function of time, are presented in Figure 26 and Figure 27, respectively.

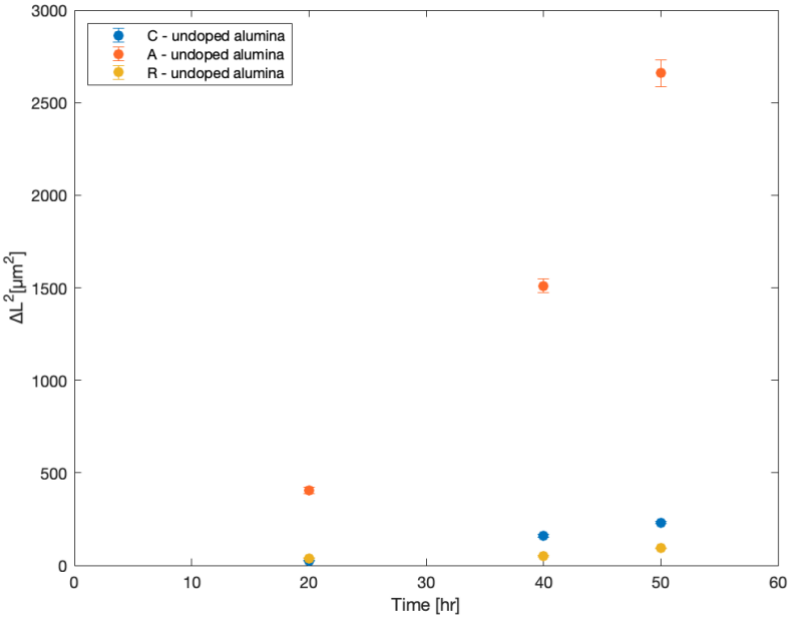

Figure 26: Grain growth kinetics of the *C*, *A*, and *R* – oriented single crystals sapphire diffusion bonded to *undoped* alumina at 1600°C.

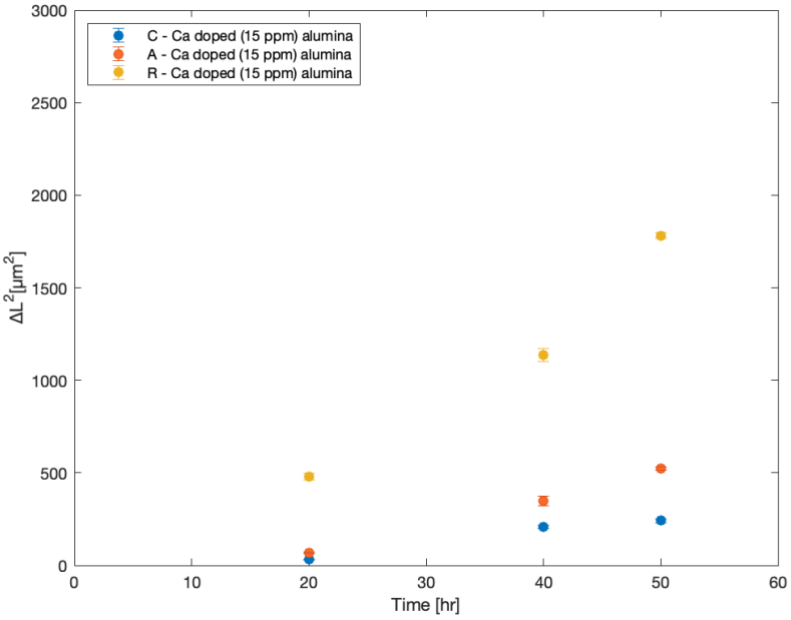

Figure 27: Grain growth kinetics of the *C*, *A*, and *R* – oriented single crystals sapphire diffusion bonded to *Ca-doped* alumina at 1600°C.

The presented figures show that for undoped alumina *A* has the largest displacement into the undoped alumina, followed by *C* and then *R*. In Ca-doped alumina; R has the largest displacement, followed by A and then C. The effective mobilities of the single crystals

were determined from the squared displacement as a function of time, using Equation (21), and are presented in Table 2.

Table 2: Summary of the effective single crystal mobility measured for undoped, and Ca-doped alumina at 1600°C.

Plane	Effective Mobility 10^{-16} $[\frac{m^2}{sec}]$	
	Undoped alumina	**Ca-doped alumina**
C (0001)	7.5 ± 2	17.5 ± 0.5
A $\{11\bar{2}0\}$	24.3 ± 0.7	25.1 ± 0.7
R $\{\bar{1}012\}$	3.6 ± 1	42.5 ± 1

The effective grain boundary mobilities are consistent with the displacements presented in Figures Figure 26 and Figure 27. In undoped alumina, the *A* plane has the highest mobility, followed by *C* and then *R*. In Ca-doped alumina the *R* plane has the highest mobility, followed by *A* and then *C*.

The presented results show that in Ca-doped alumina at 1600°C, compared with undoped alumina, the effective mobility of the *C* plane increases, the effective mobility of the *A* plane doesn't change, and the effective mobility of the *R* plane significantly increases.

In the case of undoped alumina, the effective mobility of the *A* plane was found to be higher than the mobility of the other two planes, but no elongated grains morphology is observed in undoped alumina, suggesting that the elongated grains morphology is mainly dominated and controlled by the mobility of the *C* and *R* planes.

4.5 The Equilibrium Crystal Shape of Alumina

4.5.1 Time Required to Reach Equilibrium

In order to study the effect of Ca on the ECS of alumina, the time required to reach equilibrium was estimated as explained in 3.2.6.

Figure 28 presents an example of an annealed hole, annealed in air at 1600°C, for 3 h, 11 h, and 23 h. The measured lengths L_A and L_B are indicated and the ratio ($\frac{L_A}{L_B}$) as a function of time is presented in Figure 29, from which the time required to reach equilibrium at 1600°C was estimated to be 20 h.

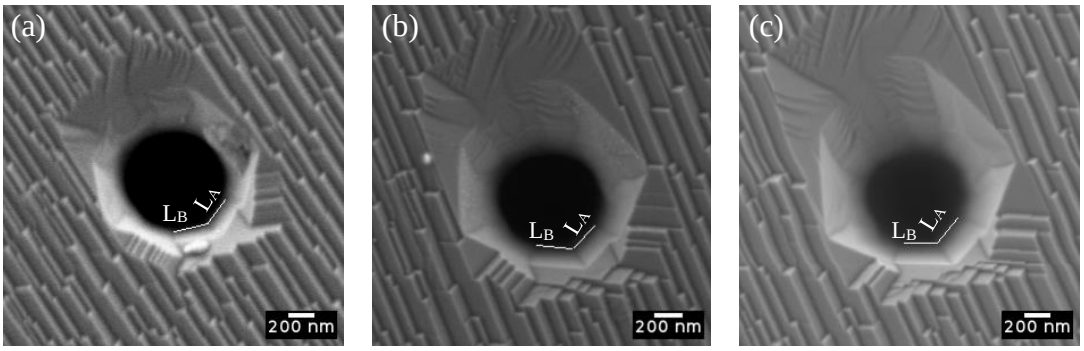

Figure 28: SE SEM micrographs of a hole fabricated in polycrystalline Ca-doped alumina annealed in air at 1600°C for (a) 3 h, (b) 11 and (c) 23 h.

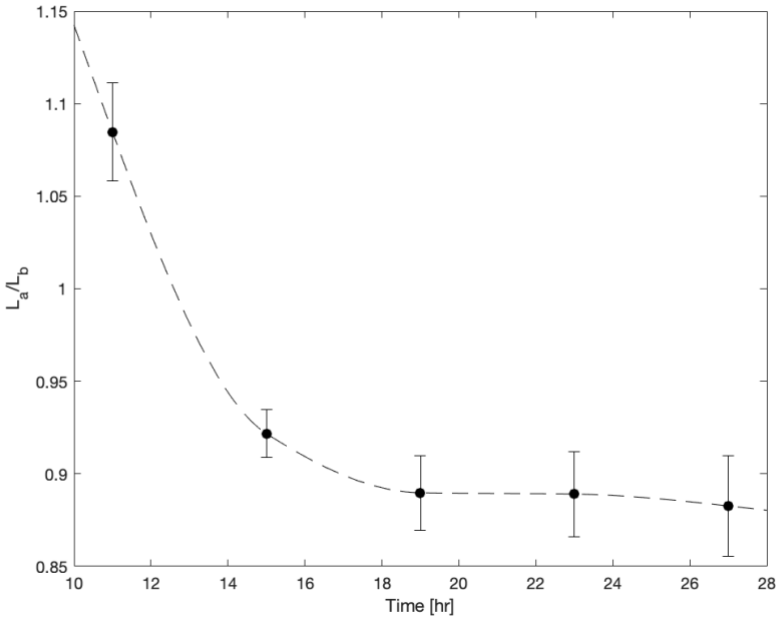

Figure 29: Ratio $\frac{L_A}{L_B}$ as a function of time, for a hole annealed at 1600°C. The dashed line is only a guide to the eye.

4.5.2 Relative Surface Energy Estimated from Internal Cavities in Ca-Doped Alumina

Holes fabricated in polycrystalline Ca-doped alumina were studied in order to understand the effect of Ca on the ECS of alumina. The holes were fabricated in selected grains with known orientation.

The orientations of the polycrystalline grains were acquired from EBSD mapping as explained in section 3.2.7. Figure 30 presents an EBSD map of a specific area in polycrystalline Ca-doped alumina, where a grain with an orientation close to the *A* plane (in green) was selected for hole fabrication.

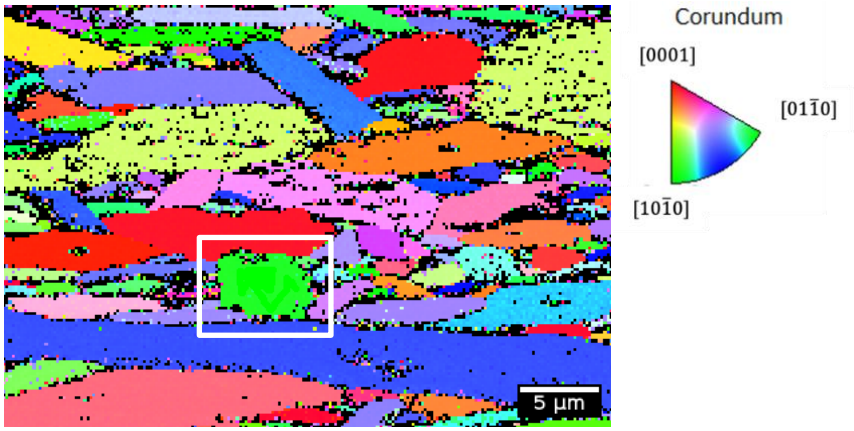

Figure 30: EBSD map in polycrystalline Ca-doped alumina sample. An A-oriented grain, in which a hole was fabricated, is indicated with a white rectangle.

Figure 31 presents a micrograph of a hole fabricated in the selected grain, annealed for 20 h at 1600℃, in which faceted edges are observed. The direction in which the hole was cross-sectioned is indicated (line O).

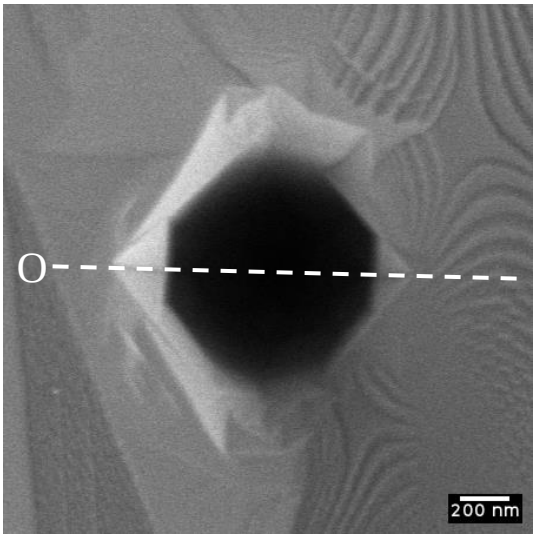

Figure 31: SE SEM micrographs of a hole in an A-oriented polycrystalline Ca-doped alumina grain, annealed at 1600°C for 20 h.

A cross-section of the hole in Figure 31 is presented in Figure 32, where the observed facets and their perpendiculars are indicated in the figure. It can be seen from the figure that not all perpendiculars meet at the same intersection point, since not all facets are edge-on to the viewing direction. Facets not edge-on were not included in the ECS analysis.

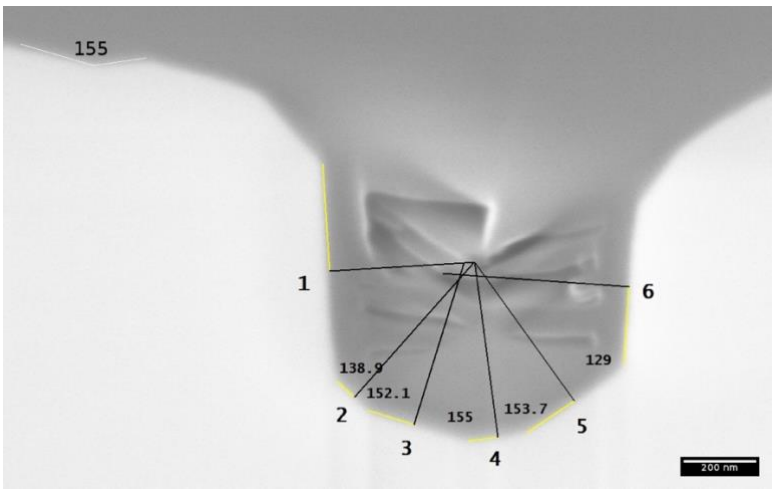

Figure 32: SE SEM micrographs of a cross-section of the annealed hole. The observed facets and their perpendiculars are marked.

Since the surface of the grain is close to the *A*-orientation, angle measurements were used to identify the observed facets, and a comparison with a simulated ECS of alumina was done for confirmation. A simulated ECS of alumina is presented in Figure 33, which was simulated using the Krystal Shaper software using relative surface energies reported in the literature by Choi et al. [22].

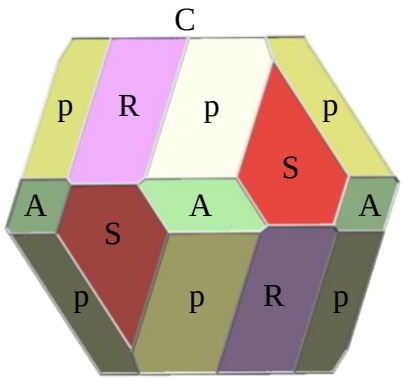

Figure 33: A simulation of the ECS of undoped alumina, produced using Krystal Shaper software, using relative surface energies reported from the literature [22].

Facet 1 has the largest area, this facet is assumed to be in the *C* plane orientation, since the *C* plane is perpendicular to the *A* plane and expected to have the lowest energy [21-25], hence the largest area, as seen in the ECS.

The upper surface of the grain appears to be faceted, and the angle between two facets is equal to the angle between facets #3 and #4 indicated in the figure, meaning that the base of the equilibrated hole is in the same orientation as the surface of the grain, as expected. The identified facets are summarized in the Table 3.

The relative surface energies of the facets were estimated by measuring the ratio between the length of the perpendiculars, following the Wulff construction [37]. The estimated relative surface energies, relative to C plane (facet #1) are presented in Table 3.

Table 3: Summary of the identified facets and their estimated relative surface energies.

Facet	Plane	Relative surface energy $\frac{\gamma_i}{\gamma_1}$
#1	***C*** (0001)	1 ± 0.0003
#2	***P*** $\{11\bar{2}3\}$	1.26 ± 0.0004
#3	***S*** $\{1\bar{1}01\}$	-
#4	***A*** $\{11\bar{2}0\}$	1.22 ± 0.0005
#5	***P*** $\{11\bar{2}3\}$	1.18 ± 0.002
#6	-	-

The estimated relative surface energies are consistent with the acquired cross-section, looking at facets #2, #4, and #5; #2 has a small area, #4 has a larger area, and #5 has the largest area. The estimated relative surface energy for #2 is the highest, then #4, then #5, meaning; the larger the area of a facet, the lower its surface energy, which is expected according to Wulff [37].

Facets #2 and #5 have the same plane orientation, but the estimated relative surface energy is not the same, since the grain is tilted, and the cross-section does not cut through the total area of the two P facets. If the orientation of the grain is completely parallel to the A plane, we would expect the equilibrated hole to have only three facets at the base.

Figure 34 presents a micrograph of another hole, fabricated in a grain with an orientation also close to *A* plane orientation, annealed at 1600°C for 20 h. The direction in which the hole was cross-sectioned is marked on the figure.

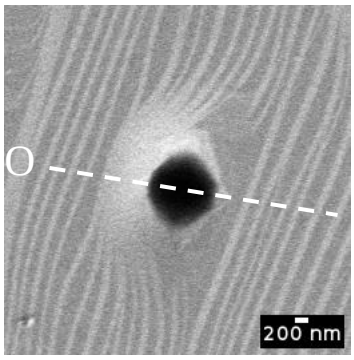

Figure 34: SE SEM micrographs of a hole in a grain in polycrystalline Ca-doped alumina, annealed at 1600°C for 20 h.

The acquired cross-section is presented in Figure 35, and the observed facets, their normals and the measured angles are marked.

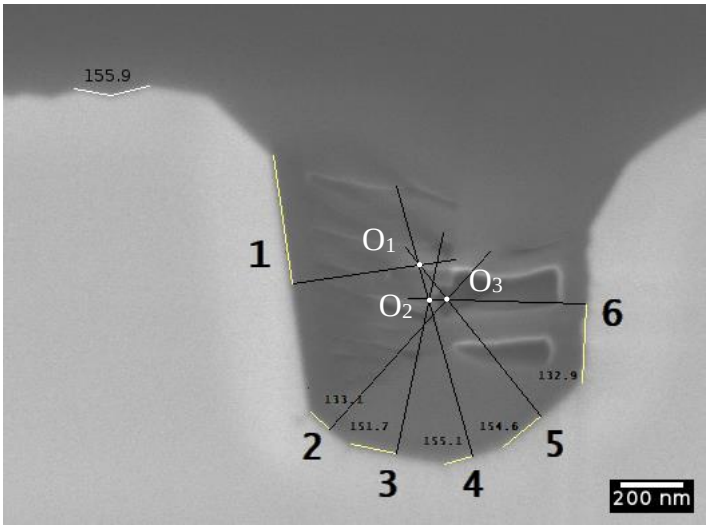

Figure 35: SE SEM micrographs of the cross-section of the annealed hole in Figure 34. The observed facets and their normal are marked.

Similar to the previous case, the base of the equilibrated hole (facets #3 and #4) and the surface of the grain are faceted, and the angle between each two facets is the same.

Since the orientation of the grain is close to the orientation of the grain presented in the previous case (Figure 32), the observed facets and measured angles are also relatively similar.

While the perpendiculars meet at three different intersection points; the relative surface energies were estimated for facets #1, #4 and #5 (from point O_1), relative to facet #1, and the results are presented in Table 4.

Table 4: Summary of the identified facets and their estimated relative surface energies for the hole presented in Figure 35.

Facet	Plane	Relative surface energy $\frac{\gamma_i}{\gamma_6}$
#1	***C*** (0001)	1 ± 0.008
#2	***P*** $\{11\bar{2}3\}$	-
#3	***S*** $\{1\bar{1}01\}$	-
#4	***A*** $\{11\bar{2}0\}$	1.55 ± 0.007
#5	***P*** $\{11\bar{2}3\}$	1.52 ± 0.007
#6	-	-

The estimated relative surface energies values differ from the ones measured from the hole presented in Figure 32, but the same trend is observed, facets oriented parallel to the C-plane have the lowest energy, followed by facets parallel to the P-plane, and facets parallel to A-plane have a higher relative energy.

Considering the elongated shape of Ca-doped alumina grains, as the holes are an "inverse" representation of the equilibrium shape, the results acquired from the second hole of Ca-doped alumina (Table 4) could make more sense, and may indicate to that the surface energy of *C*-plane (the basal plane) is much lower as a result of Ca segregation to the specific basal plane [50].

These results should be treated carefully and more statistics are required, since the Ca content measured in the sample (15 ppm), is an average measurement from different areas in the sample, where different grains might have a slightly different Ca content. As was observed kinetically, anisotropic segregation might also occur thermodynamically or due to concentration fluctuation between grains. For example, one grain might contain a small/ neglectable amount of Ca, with little segregation to grain boundaries surfaces, while another might contain a higher Ca concentration resulting in more segregation and thus lowering the surface energy even more.

4.5.3 Relative Surface Energy Estimated from Internal Cavities in Undoped Alumina

Holes were fabricated in a grain in undoped polycrystalline alumina. The grain was chosen after confirming an orientation close to the *A*-plane orientation in order to be able to compare with the results acquired from the Ca-doped alumina cross-sectioned holes.

A cross-section of the annealed hole is presented in Figure 36, the observed facets and measured angles are marked on the figure. As was observed from previous cases, not all facets are edged on or meet at one intersection point, the identified facets and the measured relative surface energies (relative to facet #4), according to point O_1, are listed it Table 5.

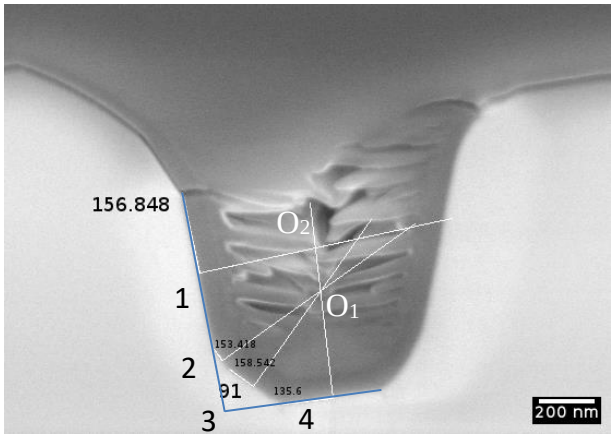

Figure 36: SE SEM micrographs of a cross-section of an annealed hole in undoped alumina. The observed facets and their normal are marked.

Table 5: Summary of the identified facets and their estimated relative surface energies for the hole presented in Figure 36, calculated from intersection point O_1.

Facet	Plane	Relative surface energy $\frac{\gamma_i}{\gamma_4}$
#1	***C*** (0001)	-
#2	-	1.150 ± 0.007
#3	***S*** $\{1\bar{1}01\}$	1.108 ± 0.007
#4	***A*** $\{11\bar{2}0\}$	1 ± 0.009

Although the orientation of the grain is close to the ones presented in 4.5.2, for Ca-doped alumina, not all facets are observed, and some appear curved, as observed in Figure 36. Moreover, facet #2 was not identified by its angle from the other planes, although it is edge on with facets #3 and #4.

Since the *C*-plane oriented facets are observed in the previous cases of Ca-doped alumina grains, in order to be able to compare, another measurement of the relative surface energy was done using O_2 intersection point, the results are presented in Table 6.

Table 6: Summary of the identified facets and their estimated relative surface energies for the hole presented in Figure 36, determined from intersection point O_2.

Facet	Plane	Relative surface energy $\frac{\gamma_i}{\gamma_1}$
#1	***C*** (0001)	1 ± 0.009
#2	-	-
#3	-	-

#4	$\boldsymbol{A}\ \{11\bar{2}0\}$	1.23 ± 0.004

Facets parallel to the *A*-plane have a higher surface energy than facets parallel to *C*-plane, which was also observed for equilibrated holes in Ca-doped alumina. Comparing the values of the relative surface energies; the relative surface energy of *A*-plane in undoped alumina is close to the one measured from the first Ca-doped hole (Table 3), but the one measured for the same facet in the second Ca-doped hole is much higher (Table 4).

As mentioned earlier, planes were identified by measuring angles relative to the known orientation of the grain and by comparing them to the known equilibrium crystal shape of alumina. However, the grain orientations are not perfectly aligned with specific planes, and, as was observed surface faceting occurs after prolonged annealing at high temperature. This approach is therefore less accurate than working with single crystals od well-defined orientation. As a result, the identification of the observed planes may be inaccurate are requires further investigation to be statically meaningful.

5. Discussion

5.1 Grain Boundary Motion

5.1.1 Effective Grain Boundary Mobility of Undoped and Ca-Doped Alumina

The increased effective mobility in the Ca-doped polycrystalline alumina, relative to undoped alumina, is in agreement with previous works [12-16,31,32]. Ignoring studies where the actual Ca content was not measured, Akiva et al. and Moshe et al. reported an increase in the effective mobility for Ca doped alumina which was experimentally confirmed to be at concentrations below the solubility limit [13,31].

While Mg also segregates to the grain boundaries and is known to decrease the effective grain boundary mobility [26-29,31], this phenomena was explained using the solute-drag effect [11]. The increased mobility in Ca-doped alumina contradicts the solute-drag effect, and demonstrates that solute-"acceleration" is also possible and happens as a result of atoms segregating to the grain boundaries.

In their attempt to understand the increased mobility in Ca-doped alumina, Dillon and Harmer claimed that the increase in the mobility, as a result of Ca segregation, is due to a first order complexion transition (Figure 37) at the grain boundary, altering the grain boundary structure and/or the chemical content [12]. In their work Dillon and Harmer did not measure the actual Ca content, and they may have had secondary phases (indicating a concentration above the solubility limit, where precipitates would be expected to influence the mobility of grain boundaries). Even below the solubility limit, simply stating that this transition results in an increased mobility does not explain how the mechanism is affected.

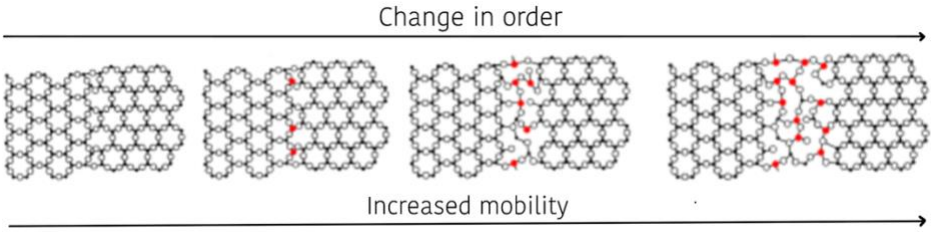

Figure 37: Schematic showing the effect of different amounts of disorder within the core of a grain boundary on the grain-boundary mobility, reproduced after [12].

Disconnections at the grain boundary are considered to be the main mechanism by which grain boundaries move [7]. Sternlicht et al. demonstrated through both ex-situ and in-situ observations of general high-angle grain boundaries in $SrTiO_3$ that grain boundary migration occurs via the movement of disconnections, and that these disconnections exhibit a strong directional dependence, making them highly anisotropic. Sternlicht et al. further demonstrated that higher temperatures can activate additional types of disconnections [8]. This finding was supported by the simulations of Han et al. [41].

If we try to explain the effect of atoms segregating to grain boundaries and influencing disconnections, Figure 38 (a) and (b) present a schematic drawing describing Gibbisian segregation to a general high angle grain boundary. Figure 38 (a) presents a typical grain boundary in a polycrystalline matrix, containing typical defects such as vacancies and impurities, with no apparent solute segregation to the grain boundaries, showing one type of disconnections present at the grain boundary (D1).

Figure 38 (b) presents the case of doping with atoms which do segregate to the grain boundaries, resulting in change in the composition of the disconnections at the grain boundary, and also in a new structure by changing the order. As a result, additional types of disconnections are present (D2).

The appearance of additional types of disconnections as a result of the change in the structure and in the composition, can indicate that atomic segregation might change the activation energy required to create some types of disconnections. This is in line with the concepts explored by Han et al. [9].

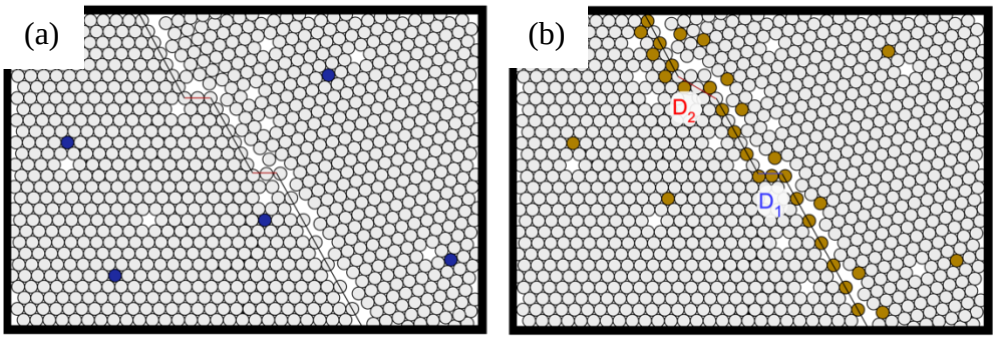

Figure 38: (a) Schematic drawing of a general grain boundary in a polycrystalline matrix presenting (a) ideal system with no segregation, with one type of disconnection, and (b) adsorption to the grain boundary resulting in additional type of disconnection (D_2) .

Taking the case of solute drag, Mg for examples segregates to grain boundaries in alumina. This segregation may result in increasing the activation energy required to create some types of disconnections, resulting in less disconnections at the grain boundaries and thus reduced grain boundary mobility.

In the case of Ca, segregation to the grain boundaries may result in decreasing the activation energy required to create some type of disconnections. As a result, more types of disconnections might be present at the grain boundaries, resulting in more grain boundary motion and increased grain boundary mobility.

Besides affecting the activation energy to form disconnections, atomic segregation might lead to a change in the mobility of disconnections already present at the grain boundaries. First order complexation transitions at the grain boundary, which leads to changing the composition and/or structure of the boundaries and thus the disconnections, might result in a decreased or in an increased mobility [41].

The change of order at the grain boundaries was qualitatively studied by Dillion et al. [33] By studying complexions at the grain boundaries, they believe that these complexions influence the kinetic behavior of the material, since significant changes in grain boundary entropy (order) occur while the enthalpy remains relatively constant across various complexions. They suggested that by controlling the complexion of grain boundaries in alumina, it is possible to alter transport kinetics by several orders of magnitude, which can be achieved by adjusting the material's chemistry.

Figure 39 presents the effective grain boundary mobility as a function of dopant concentration for a *single grain boundary* in a polycrystalline system, showing two distinct behaviors: solute-catalyzed mobility at low dopant concentrations, and Zener drag at high concentrations.

The figure demonstrates that as a result of atoms segregating to the grain boundary, at concentrations below the solubility limit, in a system with solute drag phenomena (in blue), a first order complexion transition might result in either a further decrease of the mobility of a grain boundary, or in an increase of the mobility. In the case of solute- "acceleration" (in red), a first order complexation transition might result either in an increase in the grain boundary mobility, or in a decrease of the mobility.

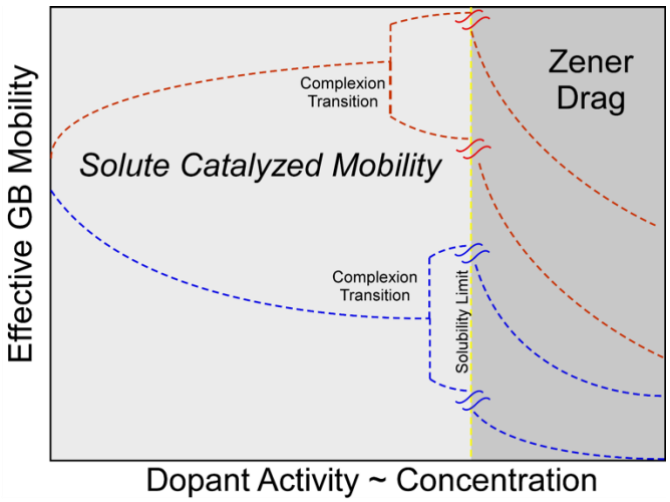

Figure 39: Schematic drawing of effective grain boundary mobility as a function of dopant concentration for a single grain boundary in a polycrystalline matrix.

In polycrystalline materials, given the many different types of grain boundaries, first order complexion transitions would be expected to occur *over a range of solute activity* (Figure 40). In this case we talk about the average grain boundary mobility, which could be affected in a similar way. For solute-drag, first order complexion transitions might result in a decrease in the averaged grain boundary mobility or in an increase of the averaged grain boundary mobility. For solute- "acceleration", the average grain boundary mobility might increase or decrease as a result of the transition.

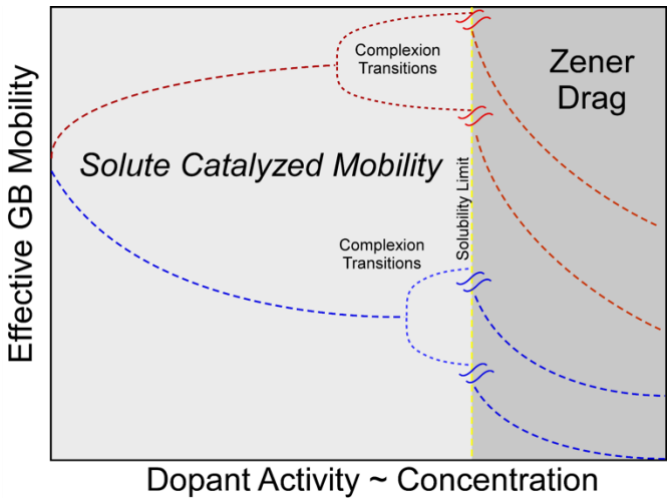

Figure 40: Averaged effective grain boundary mobility as a function of adsorbing dopant concentration in a polycrystalline system.

For the case of Mg, its adsorption to the grain boundaries of alumina at concentrations below the solubility limit either hinders the movement of disconnections in the planes of the grain boundaries, and/or increases the activation energy required to form some types of disconnections. As a result, Mg segregation decreases the grain boundary mobility.

Since Ca segregation to the grain boundaries increases the mobility at a concentration below solubility limit, atoms at the grain boundaries are either changing the structure and/or composition of the disconnections, leading to an increase in the lateral movement of the disconnections in the plane of the grain boundaries, or decreasing the activation energy required to create some types of disconnections, resulting in more grain boundary motion and increased grain boundary mobility.

Atkinson, Grimes, and Lagerlöf used atomistic computer simulations to explore the defect chemistry of alumina [42-44]. Their findings indicated that in most cases, the lowest energy mechanism for divalent ion substitution (e.g. Ca^{2+} replacing Al^{3+}) includes charge compensation by oxygen vacancies, while for Mg self-compensation is preferred, probably due the difference in ion size.

Considering the charge compensating mechanism for Mg in alumina to be self-compensating interstitials:

$$3MgO \leftrightarrow 2Mg'_{Al} + Mg_i^{\cdot\cdot} + 3O_O^x \quad (23)$$

Mg is known to decrease the grain boundary mobility via solute-drag. It may be that self-compensating Mg^{+2} interstitials increase the activation energy to form disconnections, or pins existing disconnections and thus hinders their motion.

The accepted charge compensating mechanism for Ca in alumina is:

$$2CaO \leftrightarrow 2Ca_{Al}^{\cdot} + V_O'' \quad (24)$$

where Ca^{2+} replaces Al^{3+}, and as a result O^{2-} vacancies form. Thus, Ca segregation results in an increase in the number of the oxygen vacancies at the grain boundaries, presumably affecting the structure and/or the composition of disconnections at these grain boundaries, and as a result, influencing either their mobility or the activation energy required to create them, resulting in an increased effective grain boundary mobility in Ca doped alumina. The exact mechanism by which Ca and its charge compensating defects affects grain boundary mobility is still unknown, but our hypothesis is that oxygen vacancies affect the increased mobility of the disconnections, and the increased grain boundary mobility.

In both cases dominant types of disconnections might be present, and their associated activation energies for motion might differ [41], thus further analysis of types of disconnections at the grain boundaries as a function of composition are required.

5.1.2 The Effect of Surface on Grain Size Measurements and Grains Morphology

Many studies in the literature reported results and conclusions based on measurements done from the surface [45-48]. In some works grain size measurements may not be critical for the conclusions, for example; Goa et al. reported more uniform and dense grain structure from grain size measurements with increased temperature [45], which is expected at high temperatures. In other works, the reported conclusions may not be accurate and should be treated carefully, for example, Wang et al. reported an increased grain size with an increase of $BiScO_3$ concentration in $Bi_{0.5}Na_{0.5}TiO_3$ [47], this could be

the case, but the results in this work show that different behavior is observed at the surface of alumina, in terms of kinetics and microstructure, which suggests a different amount of Ca might be present at the surface compared with the bulk. Further measurements of the concentration should be done in order to confirm this conclusion.

The measured difference in the grain boundary mobility might be attributed to surface parameters, other than the amount of Ca atoms. One possible explanation might be due to the fact that the samples were polished and thermally etched prior to the annealing process. As a result, grain boundary grooves were present at the surface of the samples and these grooves are expected to hinder grain boundary motion by pinning them. This effect was studied and explained by Mullins [49], where the key result is that if the angle between the grain boundary and the surface is too small, the boundary will get "stuck" and won't move smoothly. This critical angle is a threshold parameter that prevents the boundary from continuing its movement. Experimental evidence is also provided, showing that these grooves slow down the movement of grain boundaries at the surface, causing the motion to be jerky instead of continuous.

5.1.3 Anisotropic Grain Boundary Mobility of Ca-Doped Alumina

The results in this work show that that while Ca is known to increase the effective grain boundary mobility in alumina, the increase is anisotropic. This was indicated by previous studies [12,15,31,32].

Akiva et al. confirmed a correlation between Ca (30 ppm) and the presence of elongated grains, with an increase in the mobility of the basal plane. While their findings did not explain the elongated grain morphology, it was assumed that Ca increases the effective mobility of the non-basal planes more than that of the basal plane [31].

The results presented here are in agreement; elongated grains are observed after long annealing durations for samples doped with 15 ppm of Ca. Ca was demonstrated to increase the mobility of the basal plane, and even more so the rhombohedral plane. This suggests that the morphology of Ca-doped alumina is kinetically controlled by the

anisotropic mobility of the grain boundaries, and not only by anisotropic grain boundary energy due to Ca adsorption.

Considering disconnections and complexions at the grains boundary, the results suggest either anisotropic Ca segregation, where different amounts of Ca atoms might be segregating to each grain boundary plane/orientation and that might lead to different effects on the types and/ or the mobilities of the disconnections present at these grain boundaries. Or, that Ca has an anisotropic effect on the disconnections mobilities for different planes. For that, chemical analysis of Ca excess at different grain boundary orientations is required.

5.1.4 The Mobility of the Basal Plane (0001)

The long axis of elongated grains in Ca doped alumina are known to be parallel to the basal (C) plane [50], which is known to be the lowest energy plane in alumina [21-25]. As a result, many concluded that the elongated grain morphology was energy driven. However, Akiva et al. and now this study showed that the effective mobility of the basal plane increases due to Ca adsorption, in addition to a decrease in grain boundary excess energy [31]. This indicates that low surface/grain boundary energy does not necessarily mean low grain boundary mobility.

Considering the morphology of the elongated grains, one would expect that the mobility of the basal plane decreases rather than increases. Instead, while the basal plane's mobility increases, the mobility of the prismatic and even more so the rhombohedral planes dominate the kinetics of grain growth. This suggests that the anisotropic mobility is a result of anisotropic segregation of Ca (or the anisotropic influence of segregating Ca on disconnections at different planes), and this controls the morphology of the crystal shape, resulting in elongated grains. It also appears that under the influence of Ca, the mobility of the rhombohedral plane is dominant.

5.1.5 The Mobility of Non-Basal Planes

Finkelstein et al. and Glozman reported higher mobilities for the prismatic plane, compared with the basal plane [51,52]. The results here are in agreement in both undoped

and Ca-doped alumina (~x3.5, and ~x1.5 higher in undoped, and in Ca-doped alumina, respectively).

Considering the facts that no elongated grains were observed in the undoped polycrystalline alumina samples, even with higher mobility for the prismatic plane, and the fact that the mobility of the prismatic plane did not change due to Ca doping, emphasizes the assumption that the increased mobility of the rhombohedral plane is dominant and controlling the morphology of the elongated grains in Ca doped alumina.

The results further emphasize the importance of understanding the kinetic crystal shape (KCS), along with the equilibrium (energy-driven) crystal shape (ECS) in polycrystalline ceramics. Previous works in the literature, reported that the actual shape of the crystal is a combination of both the equilibrium crystal shape (ECS) and the kinetic growth shape (KCS) [53-55].

5.1.6 Sapphire Single Crystal Morphology at the Interface of Diffusion Bonded Samples

The flat interface of the basal plane, and the curved morphology of the prismatic plane were observed in previous works in alumina, strontium titanate, and other ceramic materials [56-59].

In their observations in strontium titanate Rheinheimer et al. state that the morphology corresponds well with the morphology of the observed abnormal grains in the polycrystalline samples. Moreover, they state that during annealing faster growing orientations break up into macroscopic facets composed of slower growing orientations [58,59].

In this work, the results show that during annealing, the interface of the basal plane-oriented sapphire, bonded to undoped alumina, remained flat and uniform, while the growth of the prismatic and rhombohedral planes resulted in a “wavy” interface. The mobility of the prismatic plane was measured to be the highest in undoped alumina, and this could explain the wavy behavior, but the mobility of the rhombohedral plane is relatively slow, and it still showed a wavy interface.

In Ca-doped alumina the mobility of the basal plane was measured to be the lowest, and it still maintained a flat interface. The rhombohedral plane also showed a flat interface although its mobility was measured to be very high. Based on statements made by Rheinheimer et al., one would expect it to have a wavy interface due to it kinetically forming slower growing orientations, but this was not the case.

The observed results suggest that the morphology of the interface of the diffusion bonded samples is not only related to the mobilities of the single crystals. The different behavior of the rhombohedral plane, in undoped and in Ca-doped alumina, further emphasizes the assumption that Ca segregation might have a different effect on different grain boundaries, or on different plane orientations, which might lead to different morphologies due to the presence of specific disconnections.

5.2 The Equilibrium Crystal Shape of Ca-Doped Alumina.

In this study, polycrystalline undoped and Ca-doped alumina samples were analyzed to investigate anisotropy and the influence of Ca on the relative surface energy of alumina. The relative surface energies measured for non-basal planes (as shown in Table 3-Table 6) are higher than values reported in the literature [21-25]. Since Ca is known to segregate to the basal (C) plane in alumina [50], it likely lowers the surface energy of this plane, complicating the interpretation of increased relative surface energies in the non-basal planes. It remains unclear whether this increase is solely due to the reduced surface energy of the basal plane or if Ca directly impacts the surface energies of all planes.

These finding warrants caution, as it is based on measurements from a single site, where the grain orientation was not precisely aligned with any one plane, and faceted surfaces appeared after annealing. Additionally, as noted in Section 4.5.2, similar facets in grains with nearly identical orientations exhibited different relative surface energies, suggesting potential variations in Ca content and segregation behavior.

The anisotropy of the equilibrium crystal shape of sapphire is a well-studied system; previous works presented by Choi et al. [22] and Kitayama et al. [24,25] presented two slightly different results, where the difference is mainly tributed to the level of impurities in the polycrystalline alumina used by Kitayama et al. This shows one of the challenges with working with polycrystalline samples, which are likely to dissolve impurities during processing.

The results present some more challenges for working with polycrystalline samples; although EBSD provides information about the orientation of the grain; acquiring high-quality cross-sections with the focused ion beam (FIB) can be challenging due to the potential for imprecise cutting. The ion beam may cause unintended damage, including redeposition and surface roughening, which can complicate subsequent analysis.
Moreover, surface faceting can happen after annealing for long durations, particularly in materials like alumina. These factors combined make working with polycrystalline materials a complex task requiring attention to detail in both sample preparation and post-processing treatments.

6. Summary and Conclusions

This works presents a series of experimental methods employed to understand the effect of Ca on the elongated grain morphology observed in Ca-doped alumina.

Undoped and Ca-doped (15 ppm) polycrystalline alumina samples were prepared and carefully characterized after obtaining full denstiy and very low level of impurities (using WDS measurements). The samples were thermally annealed at 1600°C, in air, for different time durations and the grain growth kinetics were studied. The results show that Ca doping increase the effective mobility for most of the grain boundaries, where the mean effective grain boundary mobility was estimated to be $15 \cdot 10^{-16}$ m^2/sec, and $2.9 \cdot 10^{-16}$ m^2/sec for undoped alumina. While Ca is known to segregate to the grain boundaries, where it lowers the grain boundary energy, the present study experimentally demonstrates that Ca anisotropically increases the grain boundary mobility on alumina. The increase may be to Ca affecting the structure and/or the composition of disconnections at the grain boundaries.

The effective mobilities of specific planes in alumina were measured, showing that the increased mobility in Ca doped alumina is anisotropic. The results show that Ca increases the effective mobility of the basal (0001) plane, (~x2.3 increase), significantly increases the effective mobility of the rhombohedral $\{\bar{1}012\}$ plane (~ x12 increase), while the effective mobility of the prismatic plane does not change. This result indicates that the morphology of the elongated grains in Ca-doped alumina is controlled by the kinetics of grain boundary motion.

Internal cavities were fabricated in Ca doped alumina grains with a known orientation, and used to determine the time required to reach equilibrium, which was estimated to be 20 h at 1600°C. These cavities are being used to understand the effect of Ca on the relative surface energy and the equilibrium crystal shape of alumina. Initial results showed a trend similar to what is reported in the literature ($\boldsymbol{\gamma_A > \gamma_P > \gamma_C}$), while the relative surface energies estimated for the A and P planes are higher in Ca-doped alumina; this could indicate that Ca lowers the relative surface energy of the basal (C) plane. Further investigations are needed to statistically confirm these later results.

7. Recommendations for Future Work

Grain growth is a fundamental process that occurs during sintering. While disconnection motion is considered to be the main mechanism for grain growth and grain boundary motion, the mechanism by which different dopants/impurities affect the structure, the composition, and the motion of these disconnections is not fully understood.

To understand how each dopant might influence disconnections formation and their motion at grain boundaries, studying types of disconnections at different grain boundaries is necessary, especially grain boundaries that are parallel to the prismatic and rhombohedral planes of alumina.

While the increased mobility is anisotropic, the results suggest either anisotropic Ca segregation to different grain boundaries, or that Ca might have a different effect on different grain boundary orientations, or both. For that, chemical analyses of Ca excess at different grain boundaries is required.

Considering the charge compensating mechanism of Ca doping in alumina, anisotropic Ca segregation would result in an anisotropic excess of oxygen vacancies at different grain boundaries. Thus, it is worth studying the effect of applying a direct electrical field during sintering, or during grain growth. If oxygen vacancies are really the key to the increased grain boundary mobility, controlling their concentration by attracting more vacancies to the negative electrode, and decreasing their number at the positive electrode, is expected to result in different grain morphologies at both sides of the sample.

Finally, the actual shape of a crystal is a combination of both the equilibrium and the kinetic/ growth shape. While Ca increases anisotropy in mobility, further surface/grain boundary measurements are required to acquire the complete equilibrium crystal shape of Ca-doped alumina and to understand the influence of Ca on the surface energy.

8. References

1. S. J. L. Lang, Sintering - Densification, Grain Growth, and Microstructure, Elsevier Butterworth Heinemann, 2005.

2. M. N. Rahaman, *Sintering of Ceramics*, Taylor & Francis, 2008.

3. J. E. Taylor, *II—mean curvature and weighted mean curvature*, A. Metal. Mater., **40** [7]:1475-1485, 1992.

4. A. Bhattacharya, A. Y.F. Shen, C. M. Hefferan, S. F. Li, J. Lind, R. M. Suter,

C. E. Krill, and G. S. Rohrer, *Grain Boundary Velocity and Curvature Are Not Correlated in Ni Polycrystals*, Sci., **374** [6564]: 189-193, 2021.

5. V. Muralikrishnan, H. Liu, L.Yang, B. Conry, C. J. Marvel, M. P. Harmer, G. S. Rohrer, M.R. Tonks, R. M. Suter, C. E. Krill III, and A. R. Krause, *Observations of Unexpected Grain Boundary Migration in* $SrTiO_3$, Sci. Mater., **222**, 2023.

6. H. Gleiter, *Theory of Grain Boundary Migration Rate*, **17** :853-862, 1969.

7. J. P. Hirth, and R. C. Pond, Steps, *Dislocations and Disconnections as Interface Defects Relating to Structure and Phase Transformations*, A. Mater., **44** [12]: 4749-4763, 1996.

8. H. Sternlicht, W.Rheinheimer, M. J. Hoffmann, W. D. Kaplan, *The Mechanism of Grain Boundary Motion in SrTiO3*, J. Mater. Sci., **51** [1]: 467-575, 2016.

9. J. Han, D. J. Srolovitz, M. Salvalaglio, *Disconnection-Mediated Migration of Interfaces in Microstructures: I. Continuum Model*, A. Mater., **227**, 2022.

10 . J. D. Powers, A. M. Glaeser, *Grain Boundary Migration in Ceramics*, I. Sci., **6**: 23-39, 1998.

11. J. W. Cahn, The impurity-drag effect in grain boundary motion, A. Metal., **10** [9]: 789-798, 1962.

12. S. J. Dillon, M. P. Harmer, *Relating Grain-Boundary Complexion to Grain-Boundary Kinetics I: Calcia-Doped Alumina*, J. Am. Ceram. Soc., **91** [7]: 2304-2313, 2008.

13. R. Moshe, W. D. Kaplan, *The Influence of CaO on Alumina Grain Boundary Mobility*, J. Eu. Ceram. Soc., **39** [4]: 1324–1328, 2019.

14. R. Akiva, A. Berner, W. D. Kaplan, *The Solubility Limit of CaO in α-Alumina at 1600°C*. J. Am. Ceram. Soc.**, 96** [10]: 3258–3264. *2013*.

15. J. Jung, S. Baik, *Abnormal Grain Growth of Alumina: CaO Effect*, J. Am. Ceram. Soc., **86** [4]: 644–649, 2003.

16. A. Altay, M. A. Gülgün, *Microstructural Evolution of Calcium-Doped α-Alumina.* J. Am. Ceram. Soc.**, 86** [4]: 623–629, 2003.

17. R. J. Brook, *Pore-Grain Boundary Interactions and Grain Growth*, J. Am. Ceram. Soc., **52** [1]: 56-57, 1969.

18. M. Hillert, *On the Theory of Normal and Abnormal Grain Growth*, A. Metal., **13** [3] , 227–238, 1965.

19. W. D. Kingery, K. K. Bowen, and D. R. Uhlmann, *Introduction to Ceramics*, Wiley, 1976.

20. D. Brandon, and W.D. Kaplan, *Microstructural Characterization of Materials*; John Wiley & Sons, 2013.

21. I. Manassidis, and M. J. Gillan, *Structure and Energetics of Alumina Surfaces Calculated from First Principle*, J. Am. Ceram. Soc, **77** [2]: 1994, 335–338, 1994.

22. J. H. Choi, D. Y. Kim, B. J. Hockey, S. M. Wiederhorn, C. A. Handwerker, J. E. Blendell, W. C. Carter, and A. R. Roosen, *Equilibrium Shape of Internal Cavities in Sapphire*, J. Am. Ceram. Soc**, 80** [1]: 62-68,1997.

23. J. H. Choi, D.Y. Kim, B. J. Hockey, S. M. Wiederhorn, J. E. Blendell, and C. A. Handwerker, *Equilibrium Shape of Internal Cavities in Ruby and the Effect of Surface Energy Anisotropy on the Equilibrium Shape*, J. Am. Ceram. Soc, **85** [7]: 1841-1844, 2002.

24. M. Kitayama, and A. M. Glaeser, *The Wulff Shape of Alumina: IV. Ti $^{4+}$ -Doped Alumina*, J. Am. Ceram. Soc**, 88** [12]: 3492-3500, 2005.

25. M. Kitayama, and A. M. Glaeser, *The Wulff Shape of Alumina: III, Undoped Alumina*, J. Am. Ceram. Soc, **85** [3]: 611-622, 2002.

26. R.L. Coble, *Transparent Alumina and Method of Preparation*, US Patent Office US3026210A, 1962.

27. S. K Roy, and R. L. Coble, *Solubilities of Magnesia, Titania, and Magnesium Titanate in Aluminum Oxide*, J. Am. Ceram. Soc, **5** [1]: 1–6, 1968.

28. S.J. Bennison, and M. P. Harmer, *Effect of MgO Solute on the Kinetics of Grain Growth in A12O3*. J. Am. Ceram. Soc**, 66** [5]: 90-92,1983.

29. J. Rödel, and A. M. Glaeser, *Anisotropy of Grain Growth in Alumina*, J. Am. Ceram. Soc., **73** [11]: 3292-3301,1990.

30. L. Miller, A. Avishai,and W. D. Kaplan, *Solubility Limit of MgO in Al2O3 at 1600°C*, J. Am. Ceram. Soc., **89** [1]: 350-353,2006.

31. R. Akiva, A. Katsman, and W. D. Kaplan, *Anisotropic Grain Boundary Mobility in Undoped and Doped Alumina*, J. Am. Ceram. Soc., **97** [5], 1610–1618, 2014.

32. S. I. Bae, and S. Baik, *Determination of Critical Concentrations of Silica and/or Calcia for Abnormal Grain Growth in Alumina*, J. Am. Ceram. Soc., **76** [4]: 1065-1067,1993.

33. S.J. Dillon, M. Tang, W. C. Carter, M. P. Harmer, *Complexion: A New Concept for Kinetic Engineering in Materials Science*, A. Mater., **55** [18]: 6208-6218, 2007.

34. W. D. Kaplan, D. Chatain, P. Wynblatt, and W. C. Carter, *A Review of Wetting versus Adsorption, Complexions, and Related Phenomena: The Rosetta Stone of Wetting*, J. Mater. Sci., **48** [17]: 5681-5717, 2013.

35. C. Herring, *Some Theorems on the Free Energies of Crystal Surfaces*, Phys. Rev., **82** [1]: 87-93,1951.

36. P. Wynblatt, and D. Chatain, *Anisotropy of Segregation at Grain Boundaries and Surfaces*, Metall. Mater.Trans. A., **38** [9]: 2595-2620, 2006.

37. G. Wulff, XXY. Zur Frage der Geschwindigkeit des Wachs- thums und der Auflösung der Krystallflächen, Cryst. Mat., **34**: 449-350, 1901.

38. A. Berner, F. Gimelfarb. and T. Ukhorskaya, *Metrological Aspects of Microprobe Analysis*, J. Anal. Chem., (Russian) **37** [2] 338–348, 1982.

39. J. I. Goldstein, D. E. Newbury, J. R. Michael, N. W. M. Ritchie, J. H. J. Scott, and D. C. Joy, *Scanning Electron Microscopy and X-Ray Microanalysis*, Springer New York, 2018.

40. R. Moshe, A. Berner, W. D. Kaplan, *The Solubility Limit of SiO_2 in α-Alumina at 1600°C*. Scripta Materialia, **86**: 40-43, 2014.

41 . J. Han, S. L. Thomas and D. J. Srolovitz, *Grain-boundary kinetics: A unified approach*, Progress in Materials Science, **98**: 386-476, 2018.

42 . K. J. W. Atkinson, R. W. Grimes, M. R. Levy, Z. L. Coull and T. English,

Accommodation of impurities in α-Al_2O_3, α-Cr_2O_3 and α-Fe_2O, J. Eur. Ceram.

Soc., **23**[16] 3059-3070, 2003.

43 . R. W. Grimes, *Solution of MgO, CaO, and TiO_2 in α-Al_2O_3*, J. Am. Ceram. Soc.,

77[2] 378-384, 1994.

44 . K. P. D. Lagerlöf and R. W. Grimes, *The defect chemistry of sapphire (α-Al_2O_3)*,

Acta Mater., **46**[16] 5689-5700, 1998.

45 . Y. Goa, Y. Zheng, X. Lu, Z. Dong, and Z. Ke, *Synthesis and microwave dielectric properties of $CaMg_2Si_3O_9$ ceramics*, J. Mater. Sci.: Materials in Electronics, **31**[9]:1-8, 2020.

46 . V.A. Lukacs, M. Airimioaei, L. Padurariu, L.P. Curecheriu, C.E. Ciomaga, A. Bencan, G. Drazic, M. Avakian, J.L. Jones, G. Stoian, M. Deluca, R. Brunner, A. Rotaru, and L. Mitoseriu, *Phase coexistence and grain size effects on the functional properties of $BaTiO_3$ ceramics*, J. Eur. Ceram. Soc., **42**:2230-2247, 2022.

47 . L. Wang, W. Bai, X. Zhao *et al., Tailoring electromechanical performance in $BiScO_3$-modified $Bi_{0.5}Na_{0.5}TiO_3$-based lead-free piezoceramics*, J. Mater. Sci.: Mater Electron, **31**:1491–1501, 2020.

48 . S. H. Yoon, C. A. Randall, K. H. Hur, *Influence of Grain Size on Impedance Spectra and Resistance Degradation Behavior in Acceptor (Mg)-Doped $BaTiO_3$ Ceramics*, J. Am. Ceram. Soc., **92**: 2944-2952, 2009.

49 . W.W Mullins, The effect of thermal grooving on grain boundary motion, Acta Metallurgica, **6** [6]: 4147, 1958.

50 . W. D. Kaplan, H. Mxillejans, M. Rühle, J. Rödel, J. and N. Claussen, *Ca Segregation to Basal Surfaces in α-Alumina,* J. Am. Ceram. Soc., **78**: 2841-2844, 1995.

51 . Y. Finkelstein, S. M. Wiederhorn, B. J. Hockey, C. A. Handwerker and J. E.

Blendell, *Migration of Sapphire Interfaces into Vitreous Bonded Aluminium Oxide*, **7**:

258-279, Ceramic Transactions, Sintering of Advanced Ceramics.

Edited by C. A. Handwerker, W.A. Kaysser, and J. E. Blendell. The American

Ceramic Society, Westerville, OH, 1990.

52 . O. Glozman, *Grain Boundary Mobility in Alumina,* M.Sc. Thesis. Technion, Haifa, Israel, 1994.

53 . J. S. Wettlaufer et al., *A geometric model for anisotropic crystal growth*, J. Phys. A: Math. Gen., **27**:5957-5967, 1994.

54 . G. Müller, J. J. Métois, P. Rudolph, *Crystal Growth - From Fundamentals to Technology*, Elsevier Science, 2004.

55 . J. E. Taylor, J. W. Cahn, and C. A. Handwerker, *I-Geometric Models of Crystal Growth,* Acta. Metall., Mater., **40**:1443-1474, 1992.

56 . W. Rheinheimer, J. E. Blendell and C, A. Handwerke, *Equilibrium and kinetic shapes of grains in polycrystals,* Acta Mater., **191**: 101-110, 2020.

57 . J. H. Back and M. J. Kim, *Migration of Corundum Crystal Basal Surfaces in a Matrix of Fine Alumina Grains and Anorthite Liqui,* J. Am. Ceram. Soc., **88** [11]: 3177–3183, 2005.

58 . W. Rheinheimer, M. Bäurer , C, A. Handwerke, J. E. Blendell, and M. J. Hoffmann, *Growth of single crystalline seeds into polycrystalline strontium*

titanate: Anisotropy of the mobility, intrinsic drag effects and kinetic shape of grain boundaries, Acta Mater., **91**: 111-123, 2015.

59 . W. Rheinheimer, M. Bäurer, M. J. Hoffmann, *A Reversible Wetting Transition in Strontium Titanate and its Influence on Grain Growth and the Grain Boundary Mobility*, Acta Mater., **101**: 80-89, 2015.

סידן וגרעינים מאורכים באלומינה

אימאן נעאמנה

סידן וגרעינים מאורכים באלומינה

חיבור על מחקר

לשם מילוי חלקי של הדרישות לקבלת התואר

מגיסטר למדעים בהנדסת חומרים

אימאן נעאמנה

הוגש לסנט הטכניון – מכון טכנולוגי לישראל

תשרי תשפ״ה חיפה אוקטובר 2024

המחקר הזה נערך בהנחיית פרופ' וויין ד. קפלן מהפקולטה למדע והנדסה של חומרים בטכניון- מכון טכנולוגי לישראל.
מחקר זה נתמך באופן חלקי על ידי הקרן הלאומית למדע (מספר מענק 2070586).

מחבר/ת חיבור זה מצהיר/ה כי המחקר, כולל איסוף הנתונים, עיבודם והצגתם ,התייחסות והשוואה למחקרים קודמים וכו', נעשה כולו בצורה ישרה, כמצופה ממחקר מדעי המבוצע לפי אמות המידה האתיות של העולם האקדמי. כמו כן, הדיווח על המחקר ותוצאותיו בחיבור זה נעשה בצורה ישרה ומלאה, לפי אותן אמות מידה.

תקציר

גידול גרעינים הינו חלק משמעותי ודומיננטי שמתרחש בזמן סנטור (sintering) של חומרים קרמיים, כשאר המורפולוגיה המתקבלת משפיעה משמעותית על תכונות החומר המתקבל.

אחד החומרים הקרמיים הנחקרים ביותר הוא אלפא-אלומינה ,(α-$Al2O3$) המשמשת לעיתים קרובות כמודל מחקרי בשל תכונותיה האופטיות והמכאניות. מחקרים רבים באלומינה הראו כי תוספים ו/או זיהומים יכולים לגרום לשינויים משמעותיים בניידות גבול הגרעינים של החומר, מה שמשפיע על קינטית גידול הגרעינים והמורפולוגיה שלהם. שינוי זה יכול להתרחש כתוצאה מסגרגציה לפי גיבס של מומסים לגבולות גרעין, המונעת על ידי הפחתת האנרגיה של גבול הגרעין.

הוכח בעבר כי סידן (Ca) באלומינה, בריכוז נמוך מגבול המסיסות, מוביל לניידות אנאיזוטרופית ומהירה יותר של גבולות הגרעין, ויוצר גרעינים מוארכים בצורת לוחיות. לא ברור אם הצורה המוארכת נובעת מהתקרבות המערכת לשיווי משקל, כלומר לצורת גביש בשיווי משקל עקב ספיחת סידן למישורים קריסטלוגרפיים מסוימים, או שמדובר בצורת קינטית שבה סידן גורם לניידות אנאיזוטרופית של גבולות גרעין.

המטרה המרכזית של מחקר זה היא למדוד את ניידות גבול הגרעין האנאיזוטרופית באלומינה עם תוספת סידן, כדי להבין האם צורת הגרעינים המוארכת שנצפתה באלומינה עם סידן נובעת מהשפעות קינטיות (ניידות גבול הגרעין). על ידי חקר התנהגות הסידן בגבולות הגרעינים, מחקר זה שואף להבהיר את המנגנונים שבאמצעותם סידן משנה את ניידות גבול הגרעין ואת הצמיחה האנאיזוטרופית של גרעיני אלומינה, ובכך לספק תובנות על השפעתו הרחבה יותר על תכונות החומר.

במחקר זה, צורת גביש בשיווי משקל באלומינה עם תוספת סידן (ברמה מתחת לגבולות המסיסות) נחקרה באמצעות חללים פנימיים. טכניקות מיקרוסקופיה יונית ואלקטרונית משולבות שימשו ליצירת חללים ראשוניים, לקביעת הגעה לשיווי משקל, ולניתוח החללים המאוזנים כדי לקבוע את צורת השווי משקל של אלומינה עם תוספת סידן. בנוסף, נבדקה גם המובילות של חד גבישים בכיווניות שונה אל תוך אלומינה מסוממת ולא מסוממת בסידן.

לשם כך, דגמי אלומינה לא מסוממת סונטרו בטמפרטורה של 1600 מעלות צלזיוס למשך שעתיים, עד לקבלת צפיפות יחסית מלאה (98%) , הדגמים עברו טיפולים תרמיים למשך 2, 4, 6, 8 ו- 10 שעות (קצב חימום/קירור 15 מעלות צלזיוס לדקה) לקבלת גידול גרעינים. ובנוסף סונטרו דגמי אלומינה מסוממת ב 15 חלקים למיליון של סידן בטמפרטורה של 1600 מעלות צלזיוס למשך שעתיים לקבלת צפיפות יחסית מלאה (97%), ועברו אותם טיפוליים תרמיים למשך 2, 4, 6, 8 ו- 10 שעות (קצב חימום/קירור 15 מעלות צלזיוס לדקה).

גודל הגרעינים נמדד אחרי ליטוש ואיכול תרמי (בטמפרטורה של 1250 מעלות צלזיוס למשך שעתיים) של חלקים שנחתכו מאזורים פנימיים של הדגמים, התוצאות הראו כי ניידות גבולות הגרעין הממוצעת בדגמי אלומינה לא מסוממת נמצאה להיות $2.9\ (\pm 0.4) \cdot 10^{-16}$ מ״ר/שנייה, בעוד כי סימום ב 15 חלקים למיליון של סידן מעלה את הניידות הממוצעת ל $15\ (\pm 2) \cdot 10^{-16}$ מ״ר/שנייה, המוביליות של אלומינה מסוממת בסידן נמדדה לפי זמני טיפול קצרים (2-6 שעות) שבהם הגידול היה שווי צירי, גרעינים מאורכים של אלומינה הופיעו אחרי טיפול ב 1600 מעלות צלזיוס למשך 8 שעות ויותר.

העלייה בניידות של גבולות הגרעין כתוצאה מסימום בסידן הוסברה על ידי שינוי המבנה/ ההרכב של disconnectionשנמצאים בגבולות הגרעין, כאשר התנועה שלהם היא המנגנון האחראי לתנועת גבולות הגרעינים. כאשר ידוע שסידן עושה סגרגציה לגבולות הגרעינים ומעלה את מספר היעדרויות החמצן כתוצאה מאיזון המטען, הטענה היא שהעלייה של מספר היעדרויות החמצן באזור גבולות הגרעינים מוביל או לירידה באנרגית האקטיבציה ליצירת disconnection, או לעלייה בניידות שלהם.

בנוסף לכך, נמדדה הניידות של גבולות הגרעינים מאזורים קרובים לפני השטח והשוואה עם הניידות שנמדדה מאזורים פנימיים בתוך הדגם, התוצאות הראו ניידות יותר נמוכה בפני השטח ומורפולוגיה שונה, כאשר אחרי 8 שעות התקבלו גרעינים מאורכים בתוך הדגמים שלא התקבלו בפני השטח. התופעה מציעה גרדיינט ריכוז של סידן, כאשר הריכוז עולה לתוך הדגם. בנוסף לכך הניידות הנמוכה בפני השטח ביחס לפנים הדגם הוסברה על ידי ה pinning effect של groovings הנמצאים בפני השטח, שמצמידים גבולות הגרעין ומאיטים את תנועתם.

התוצאה מראה ההשפעה המשמעותית של אפקטים בפני השטח על מדידות של פרמטרים שונים והמסכנות שנגזרת מהם.

לשם קביעת המוביליות של משיור הבסיס (0001), המישור הפריזמתי $\{11\bar{2}0\}$, והמישור הרומבוהידרלי $\{\bar{1}012\}$, אל תוך אלומינה מסוממת ולא מסוממת, הוצמדו חד גבישים של אלומינה (ספיר) בעלי כיווניות של כל אחד מהמישורים אל אלומינה מסוממת ולא מסוממת בטמפרטורה של 1600 מעולת צלזיוס למשך 48 שעות, על הגביש הופעל מאמץ על ידי הנחת משקל של 1 ק״ג של אלומינה מסונטרת. הדגמים המחוברים עברו טיפולים תרמיים למשך 20, 30, 40 ו- 50 שעות, ההזזה של המישור החד גביש אל תוך האלומינה נמדדה אחרי כל טיפול לפי מעקב אחרי פורות שהיו בממשק הביניים.

עבור אלומינה לא מסממת נמדדה ניידות של $7.5\ (\pm 2) \cdot 10^{-16}$ מ״ר/שנייה עבור המישור הראשי, $24.3\ (\pm 0.7) \cdot 10^{-16}$ מ״ר/שנייה עבור המישור הפריזמתי, ו- $3.6\ (\pm 1) \cdot 10^{-16}$ מ״ר/שנייה עבור המישור הרומבוהידרלי.

באלומינה מסוממת בסידן, הניידות של המישור הראשי עלתה לערך של $17.5\ (\pm 0.5) \cdot 10^{-16}$ מ״ר/שנייה, הניידות של המישור הרומבוהידרלי עלתה בהרבה לערך של $42.5\ (\pm 1) \cdot 10^{-16}$ מ״ר/שנייה, בעוד שהניידות של המישור הפריזמתי לא השתנתה ($25.1\ (\pm 0.7) \cdot 10^{-16}$ מ״ר/שנייה).

תוצאה זו מצביעה על כך שמורפולוגיית הגרעינים המוארכים באלומינה עם תוספת סידן נשלטת על ידי הקינטיקה של תנועת גבולות הגרעינים.

לשם חקירת מבנה שיווי משקל של אלומינה מסוממת בסידן, הוכנו חורים בתוך גרעינים של אלומינה מסוממת ולא מסוממת, ששמשו לקביעת הזמן הנדרש להגעה לשיווי משקל (20 שעות בטמפרטורה של 1600 מעולת צלזיוס), חורים שהגיעו לשווי משקל בגרעינים בעלי אוריינטציה ידועה נותחו לקביעת האנרגיה המשטחית היחסית של מישורים יציבים באלומינה מסוממת ולא מסוממת.

תוצאות ראשוניות מראות שאנרגית פני השטח של המישורים הלא ראשיים ביחס למישור הראשי (המישור בעל אנרגית פני השטח הכי נמוכה) באלומינה מסוממת יותר גבוהה מאשר באלומינה לא מסוממת. כאשר ידוע שסידן עושה סגרגציה למישור הראשי של אלומינה, הוא מוריד את אנרגית פני השטח של המישור לפי גיבס. ולכן עדיין לא ברור אם העלייה באנרגית פני השטח היחסית של המישורים היא כתוצאה מהשפעתו של הסידן על כל המישורים או רק על המישור הראשי. כדי לקבל את צורת שיווי משקל המלאה של אלומינה מסוממת, יותר מדידות וסטטיסטיקה נדרשת.